Author Manuscript

Planetary-scale Wave Impacts on the Venusian Upper Mesosphere and Lower Thermosphere

A. S. Brecht[1], S. W. Bougher[2], D. Shields[2], and H. Liu[3]

[1]NASA Ames Research Center, MS 245-3, Moffett Field, CA, 94035, USA.

[2]CLaSP, University of Michigan, 2418C Space Research Building, Ann Arbor, MI, 48109, USA.

[3]High Altitude Observatory, NCAR, Boulder, CO, 80301, USA.

Corresponding author: Amanda Brecht (Amanda.s.brecht@nasa.gov)

Key Points:

- Simulated planetary waves affect the atmospheric structure between 70 km and 110 km, with the Kelvin wave being dominant near the equator.
- The addition of planetary waves and a varying lower boundary can reproduce observed O_2 IR nightglow emission variability in local time.
- The simulated thermal variation due to the planetary waves does not reproduce most observed variations.

This is the author manuscript accepted for publication and has undergone full peer review but has not been through the copyediting, typesetting, pagination and proofreading process, which may lead to differences between this version and the Version of Record. Please cite this article as doi: 10.1029/2020JE006587.

This article is protected by copyright. All rights reserved.

Author Manuscript

Abstract

This work examines the planetary wave-induced variability within the upper mesosphere/lower thermosphere of Venus by utilizing the Venus Thermospheric General Circulation Model (VTGCM). Rossby and Kelvin wave perturbations are driven by variations in the geopotential height of the VTGCM lower boundary (~70 km). A suite of simulations was conducted to examine the impact of the individual and combined waves propagating from two different lower boundary conditions (uniform and varying). The Kelvin wave is the more dominant wave which produces the most variability. The combination of the Kelvin and Rossby waves provides a maximum temperature amplitude of 13 K at 92 km and maximum zonal wind amplitude of 23 m/s at 102 km. The combined waves overall are able to propagate up to 125 km. Most of the variation within the temperature, winds, and composition occurs between 70 km and 110 km. The varying lower boundary increases the magnitude of the wave deposition and atmospheric responses, but weakly changes the propagation altitude. The thermal variation due to the planetary waves does not reproduce most observed variations. The simulated O_2 IR nightglow emission is sensitive to the waves with respect to intensity and local time, but lacks latitudinal variation. The integrated intensity ranges from 1.2 MR to 1.65 MR and the local time ranges from 0.33 local time to 23.6 local time. Overall, planetary waves do affect the atmospheric structure, but there are still large observed variations that planetary waves alone cannot explain (i.e. thermal structure).

Plain Language Summary

Venus' atmosphere has a cloud layer (~40 km - ~70 km) that encompasses the whole planet that separates the lower atmosphere and upper atmosphere. Images of the clouds show planetary scale wave patterns that exist from the equator to mid-latitudes and are thought to be a

This article is protected by copyright. All rights reserved.

combination of Kelvin and Rossby waves. This work examines how the Kelvin and Rossby wave change the upper atmosphere by using a general circulation model of the upper atmosphere (~70 km - ~300 km altitude). More specifically, this project analyzes the wave induced variations in temperature, winds, and a few chemical species. This work also examines how a simplified connection to the lower atmosphere changes the behavior of the Kelvin and Rossby waves and thus variations in the upper atmosphere. The results of this work demonstrate that waves provide variations between ~70 km and 110 km altitude and are sensitive to the simplified lower atmosphere connection. The wave induced variation does not reproduce observed thermal variations but it does reproduce observed O_2 IR nightglow intensity variation. Overall, planetary waves do affect the upper atmosphere but do not propagate high enough in the atmosphere to provide all the observed variations.

1 Introduction

The Pioneer Venus Orbiter (PVO) and Venus Express (VEX) have been the two longest missions to orbit Venus and provide the largest collection of measurements. These observations have also been supplemented with observations from shorter duration orbiters, fly-bys, and ground based observations. Certain observed features have enough data to create averaged profiles or even statistical averaged maps, such as temperature, density, and nightglow emissions.

Limaye et al. (2017) has organized the available thermal profiles of Venus, from ground-based observations to probes to orbiters (VEX being the latest one). Their work is in support of upgrading the original empirical models (VIRA and VTS3); based mainly upon PVO observations (Hedin et al., 1983; Keating et al., 1985). The observations vertically cover altitudes from 40 km to 180 km and were binned into five latitude bins and three local time bins with the assumption of hemispheric symmetry. Overall, there is a large amount of variability in the temperatures and

This article is protected by copyright. All rights reserved.

Author Manuscript

densities above ~100 km. However, all the observations do demonstrate some consistent features such as warming and cooling layers. Limaye et al. (2017) also organized all the total neutral number density profiles from the various VEX observations. The terminator and nightside profiles extend from 40 km to 140 km, while the dayside profiles range from 40 km to ~90 km. In general, when multiple observations overlap vertically the density was in good agreement. Another highly observed feature in Venus' atmosphere includes nightglow emissions. From VEX observations, a statistical averaged map of the O_2 IR nightglow emission was created. The O_2 IR emission statistically appears near midnight near the equator at ~97 km (e.g. Gérard et al., 2008; Soret et al., 2012), but the map also shows considerable variation in location and intensity. These averaged fields are important for understanding the global mean climatology of Venus, while providing a gauge for comparison with numerical model simulations.

From a modeling approach, it is useful to have a larger collection of observations to provide statistical means due to the difficulty of simulating all the individual sources of temporal and spatial variability within the Venus atmosphere. The climatological view of a few key features (i.e. the nightside warm temperature layer, the O_2 IR nightglow emission, and the NO UV nightglow emission) has been analyzed using numerical models, specifically general circulation models (e.g. Bougher et al., 1990; Bougher & Borucki, 1994; Brecht et al., 2011; Gérard et al., 2017). Our work begins to expand upon climatological studies and investigates sources of variability, such as planetary waves.

Individual sources of variability are important to understand in Venus' atmosphere to help quantify the disturbances around the mean observations. Waves are abundant and a known source of variability, but their characteristics and behavior are not well known in the Venusian atmosphere. The impact of waves have been observed in many ways: neutral density (e.g.

This article is protected by copyright. All rights reserved.

Author Manuscript

Kasprzak et al., 1988; Niemann et al., 1980), temperature (e.g. Counselman et al., 1980; Hinson & Jenkins, 1995; Kliore & Patel, 1980; Kolosov et al., 1980; Seiff et al., 1980; Tellmann et al., 2012), emissions (non-LTE and nightglow) (e.g. Altieri et al., 2014; García Muñoza et al., 2009), and imaging (thermal and cloud) (e.g. Belton et al., 1976; Bertaux et al., 2016; Fukuhara et al., 2017; Kouyama et al., 2017; Markiewicz et al., 2007; Peralta et al., 2007, 2009; Piccialli et al., 2014; Rossow et al., 1980; Titov et al., 2012). Cloud imaging is a clear way to observe waves coming from the lower atmosphere or within the cloud layer and potentially propagating to the thermosphere.

Mariner 9 was the first to glimpse the unique cloud structure and it wasn't until PVO that observations could glean cloud patterns due to waves, mainly planetary waves (e.g. Del Genio & Rossow, 1990; Rossow et al., 1990). PVO observations have been the most complete and published equatorial planetary wave analysis available. Del Genio and Rossow (1990) analyzed the cloud brightness data obtained by PVO and identified an equatorial 4-day period and a mid-latitude 5-day period wave. The waves were classified as Kelvin and Rossby waves respectively. The Kelvin wave was found to have a westward phase speed of ~15 m/s relative to the wind and the Rossby wave has westward phase speed ~-32-34 m/s relative to the wind. The Rossby wave propagation is slower than the background wind and is thus retrograding with respect to the flow. VEX has observed equatorial clouds but has had minimal wave analysis due to the orbital configuration. Nara et al (2019) utilized observations from VEX Venus Monitoring Camera (VMC) to explore the connection between the planetary-scale ultraviolet contrast and the wind field. They were able to observe 4-day and 5-day periodicities in the brightness variations. These periodicities were linked to an equatorial Kelvin wave and mid-latitude Rossby wave. They found the Kelvin wave supplied the cloud top equatorial region with dark materials and subsequently the

This article is protected by copyright. All rights reserved.

Author Manuscript

dark materials are advected poleward by the Rossby wave and mean meridional circulation. The mid-latitude jet stretches it to the tilted band structures.

The JAXA Akatsuki mission has observed the equatorial clouds in detail and has performed wave analysis (Imai et al., 2019). Imai et al (2019) utilized Akatsuki UV Imager (UVI) observations to conduct time series analysis of the 365-nm brightness and cloud-tracking wind variations. They identified a 5-day periodicity in the winds and brightness variations near mid-latitudes in both hemispheres with phase velocities near ~-35 m/s with respect to the wind. Additionally, a ~3.8-day periodicity in the zonal wind and brightness variations near the equator was identified with a phase velocity ~+/-15 m/s relative to the wind. These more recent wave analysis results are in line with previous studies. Furthermore, Nara et al (2019) utilized the Akatsuki UVI 365 nm images and Hisaki EXCEED O 135.6 nm dayglow intensities to examine the vertical coupling between the cloud tops and the thermosphere. Both datasets revealed periodicity of ~3.6 days and was attributed to a Kelvin wave. Based upon one-dimensional modeling they suggest the dayglow periodicity is related to small-scale gravity waves that are influenced by Kelvin waves. The simulated Kelvin waves did not propagate into the thermosphere (above ~110 km) due to radiative damping; in addition, the gravity waves with ~1,000 km wavelengths only reached the thermosphere on the dawnside.

The first 3D numerical study of planetary waves and tidal impacts on the upper atmosphere of Venus was by Hoshino et al (2012). They implemented thermal tides and planetary waves in their mesosphere/thermosphere general circulation model to investigate the influence these waves have upon the zonal wind and the O_2 IR nightglow emission in the upper mesosphere and lower thermosphere. The study concluded that the thermal tides are damped out below ~80 km and the Kelvin and Rossby waves could propagate up to ~130 km. However, the Rossby waves were very

This article is protected by copyright. All rights reserved.

Author Manuscript

weak compared to the Kelvin waves at the equator and caused less than 1 m/s wind velocity fluctuations. The Kelvin waves could produce a ~6-10 m/s wind velocity change. Neither wave could support the observed super-rotating winds (e.g. Gierasch et al., 1997; Hueso et al., 2015; Schubert, 1983). Moreover, Hoshino et al. (2012) developed and utilized a detailed 1-D nightglow model to understand the impact Kelvin waves had upon the O_2 IR nightglow. This resulted in Kelvin waves varying the peak nightglow emission in local time and intensity but not to the magnitudes observed by VEX. Nakagawa et al. (2013) continued the Hoshino et al. (2012) work by utilizing the same Kelvin wave and GCM set up but also included gravity waves. They examined large short-term wind velocity variations by comparing ground-based infrared heterodyne observations of Doppler wind velocities and GCM simulations. Their GCM simulations only included Kelvin waves from Hoshino et al. (2012) because it was suggested the Rossby wave, diurnal and semidiurnal tides have negligible influence on the upper atmosphere. The ground-based observations of a single emission are associated to a narrow altitude range (~110 km). The GCM comparisons at this single altitude revealed the Kelvin wave wind variability is much smaller than the observations, but the gravity waves could produce the larger wind variability.

Our work presented in the next few sections will confirm and extend the work done by Hoshino et al. (2012) (here after as H12) by utilizing the Venus Thermospheric General Circulation Model (VTGCM) (e.g. Bougher et al., 1988; Brecht et al., 2011). The differences between this VTGCM work and H12 are summarized as follows: (a) the model vertical domain is larger (VTGCM is 70 km to 300 km versus 80 km to 180 km), (b) the VTGCM O_2 IR nightglow is calculated during run time with a bit lower spatial resolution (5° lon by 5° lat versus 5° lon by 10° lat) and with finer temporal resolution of 20 seconds compared to H12, (c) Kelvin waves and

This article is protected by copyright. All rights reserved.

Author Manuscript

Rossby waves are used simultaneously in VTGCM simulation, and (d) there is a spatially varying lower boundary (versus uniform) applied in the VTGCM simulation. We want to investigate how multiple sources of variability potentially within or below the Venusian clouds (~50 km - ~70 km) can affect the upper mesosphere lower thermosphere (UMLT), including temperatures, winds, densities, and O_2 IR nightglow emission. Furthermore, this work will examine the combination of these sources to see if they generate the range of variability that has been observed in the upper mesosphere.

2 Model

The VTGCM is a 3-D finite difference hydrodynamic model of the Venus upper atmosphere (e.g. Bougher et al., 1988). It started from the National Center for Atmospheric Research (NCAR) terrestrial Thermospheric Ionosphere General Circulation Model (TIGCM) (Dickinson et al., 1981). Over the last few decades, the VTGCM has been modified and improved with the details documented in e.g. Bougher et al. (1988), Brecht (2011), Brecht et al. (2011), Brecht and Bougher (2012), Bougher et al. (2015).

The VTGCM spatial dimensions are 5° by 5° latitude-longitude grid, with 69 evenly-spaced log-pressure levels in the vertical (Zp = -16 – 18), extending from approximately ~70 to 300 km (~70 to 200 km) at local noon (midnight). The vertical resolution is half a pressure scale height, which equates to ~3-5 km. The model calculates neutral temperature, zonal velocity, meridional velocity, mass mixing ratio of specific species, vertical motion, and geopotential. The calculated major species are CO_2, CO, O, N_2 and minor species are O_2, $N(^4S)$, $N(^2D)$, NO, SO, SO_2. The major species influence the atmospheric mean mass, temperature, and global scale winds, while the minor species are passive (i.e. do not change the mean mass, temperature, or winds). Select dayside photochemical ions are carried to support the neutral chemistry (CO_2^+, O_2^+,

This article is protected by copyright. All rights reserved.

Author Manuscript

O^+, N_2^+, and NO^+). The latest ion-neutral reactions and rates used in the VTGCM are largely taken from Fox and Sung (2001).

Parametrizations for CO_2 15-µm cooling, near infrared (IR) heating, extreme ultraviolet (EUV) heating, and sub-grid processes (i.e., eddy diffusion, viscosity, and conduction) are included and discussed in more detail in Brecht et al. (2011) and Brecht and Bougher (2012). The only update is the usage of near-IR heating rates from Crisp (1986) below 100 km. Lastly, the VTGCM can capture the full range of EUV-UV flux conditions. For this work, solar minimum conditions are used (F10.7 = 70), appropriate for early VEx conditions.

Rayleigh Friction: Sub-grid scale wave effects are thought to be a source for decelerating the Venusian winds and even contributing to zonal asymmetry (Bougher et al., 2006). Currently these effects cannot be captured with the VTGCM directly and instead are prescribed using a Rayleigh friction scheme to mimic the first order wave-drag effects on the mean flow (Bougher et al., 1988; Brecht et al., 2011). Implementing gravity wave momentum deposition schemes and planetary-scale waves is part of the process to remove the usage of Rayleigh friction (e.g. Brecht et al., 2019; Gilli et al., 2017; Hoshino et al., 2012, 2013; Zalucha et al., 2013; Zhang et al., 1996). For this work, gravity waves are not implemented and planetary-scale waves are only utilized to provide a potential zonal asymmetry to the zonal wind. All of the simulations presented in this paper utilize Rayleigh friction to provide an overall zonally symmetric "deceleration" of the winds above ~110 km. The RF is prescribed as: $\lambda_{RF} = (e^{(P-Po)/2}) * 1e^{-4}$ where: Po = Zp=-1.5. This RF is applied on zonal and meridional winds and is fixed in time but varies by cos(latitude).

Updated Lower Boundary Condition: The new lower boundary for the VTGCM is set at a single pressure slice at 4.44e3 Pa (~69 km) from the Oxford Venus GCM (Lee & Richardson, 2010, 2011), hereafter called OXLB. The lower boundary consists of latitude versus longitude

This article is protected by copyright. All rights reserved.

Author Manuscript

maps for temperature, zonal wind, meridional wind, and geopotential height. The Oxford output is zonally averaged and is temporally averaged over 5 solar days so that each longitude point represents a diurnal average of the data at that fixed longitude (Figure 1). This is the varying lower boundary condition. This lower boundary change only impacts the temperature and winds up to 80 km, where the largest difference is at 70 km. The temperatures are ~8 K cooler with OXLB at the equator at 70 km, while the zonal winds are ~60 m/s faster with the OXLB.

Planetary Wave Implementation: Planetary waves are prescribed within the VTGCM by specifying periodic perturbations in geopotential height at the lower boundary (Zp=-16 or ~69 km). The geopotential height perturbation for Kelvin waves is prescribed as:

$$\Phi_{KW} = Z_o \exp\left(-\left(\frac{\theta}{30}\right)^2\right) \sin(\omega_{KW} t + k_{KW}\phi)\ (1 - \exp\left(-\frac{t}{t_o}\right))$$

where Φ_{KW} is geopotential height; Z_o is the initial amplitude; θ is the latitude; ϕ is longitude; ω_{KW} is frequency (2π/345600 [rad/s]); k_{KW} is wave number (n*2 π/360; n=1 [rad/degree]); t is time; and t_o is the ramp up time (6.91 x 10^5 [s]). The utilization of a ramp up time gradually (approximately double the wave period) prescribes the planetary wave amplitudes to mitigate numerical instabilities. The geopotential height perturbation for Rossby waves is prescribed as:

$$\Phi_{RW} = Z_o \left(\sin\left((\theta - 15)\ \frac{\pi}{60 - \frac{\theta - 60}{3}} \right) \right)^2 cos(\omega_{RW} t + k_{RW}\phi - \pi)\ (1 - \exp\left(-\frac{t}{t_o}\right))$$

where Φ_{RW} is geopotential height; Z_o is the initial amplitude; θ is the latitude (limited to $22° - 72°$ in the Northern hemisphere and $-22° - -72°$ in the Southern hemisphere with a maximum $\sim\pm 47°$); k_{RW} is wave number ($n * 2\,\pi/360;\ n = 1\ [\mathrm{rad/degree}]$); ω_{RW} is frequency (2π/432000 [rad/s]); t is time; and t_o is the ramp up time (8.64 x 10^5 [s]). Moreover, the Rossby

This article is protected by copyright. All rights reserved.

Author Manuscript

wave prescription is utilized in the Northern and Southern hemisphere by using the prescribed latitude ranges.

The initial amplitudes (Z_o) for Kelvin and Rossby waves are tuned to calculate a geopotential height similar to H12. H12 derived a perturbed geopotential height field from PVO observations at the cloud top (Del Genio & Rossow, 1990; Rossow et al., 1990). The maximum derived geopotential height fluctuation for the Rossby and Kelvin wave is 10 m and 110 m respectively (see H12 Figure 1). However, the H12 derivation of the Kelvin wave geopotential height fluctuation depended on a zero background wind speed due to the H12 model lower boundary wind being set to zero. The VTGCM has a non-zero wind lower boundary due to the implementation of the OXLB, thus 60 m/s for the background wind speed was used in the derivation (based on average wind speed near the equator of the OXLB zonal wind) of a new perturbed geopotential height field to provide a consistency with the background wind speed. From the new derived geopotential height field, 50 m is the maximum geopotential height fluctuation for the Kelvin wave.

The Rossby wave is a westward (Venus rotates east to west, westward; Sun comes up in the west and sets in the east) ~5 Earth day propagating wave bound to the mid-latitudes (~20 deg to ~70 deg North and South). The Kelvin wave is a westward ~4 Earth day propagating wave contained near the equator.

3 Results

For this work, a total of five simulations were conducted to examine the individual waves and different lower boundary conditions (uniform versus varying). These simulations are listed in Table 1 with their associated conditions/parameter changes. The wave propagation within simulations #1 through #4 will be briefly discussed focusing on the fluctuations of the thermal and

This article is protected by copyright. All rights reserved.

Author Manuscript

zonal wind due to the individual planetary waves. However, the main emphasis of discussion and analysis for this paper will be done with simulation #5. Each simulation was run for 60 Earth days, which is sufficient for these studies. The timescales of the upper atmosphere are much faster than below the clouds, therefore the model reaches a "steady state" within ~50 Earth days.

3.1 Individual Kelvin and Rossby Waves Cases

3.1.1 Temperature and Zonal Wind Fluctuations - Simulations #1 and #2

Results of the independent Kelvin and Rossby wave simulation with a uniform lower boundary (simulations #1 and #2) are briefly discussed since this case was presented and discussed in detail in H12. The VTGCM simulations used the same geopotential height amplitudes as H12 for consistency, see Table 1. Examining the fluctuations produced about a mean temperature or zonal wind provides a basis for comparison with H12 and to evaluate the wave propagation. The fluctuation calculation is done by calculating the variation between the wave period and the 60 Earth day mean.

The Rossby wave VTGCM simulation (#1) produced a maximum amplitude at the equator of 0.8 m/s at 81 km and 0.1 K at 92 km for zonal wind and temperature fluctuations respectively. The Rossby wave case produces small fluctuations since it is a mid-latitude wave and this study is focusing near the equator and the prescribed geopotential height maximum amplitude is smaller than the Kelvin wave (10 m vs. 110 m). These resultant small amplitudes are similar to the results in H12, see Table 2 for comparisons. Though the altitude of these maximum amplitudes are lower than H12. These results are expected based upon the VTGCM set up with a uniform lower boundary (LB) and the prescribed geopotential height maximum amplitude set to 10 m, as is done in H12. The difference in the altitude of the maximum amplitude is likely due to the different background atmosphere (temperature and winds).

This article is protected by copyright. All rights reserved.

Author Manuscript

The Kelvin wave VTGCM simulation (#2) produces a maximum amplitude from the zonal wind fluctuation at the equator around 89 km of 6 m/s and a maximum amplitude from temperature fluctuation of the equator around 94 km for 3.0 K for Kelvin waves. The maximum amplitudes are similar to H12 but the respective altitudes are lower. Nakagawa et al. (2013) had similar results to H12, where the maximum amplitude of the zonal wind fluctuations is ~4-5 m/s and at altitude of ~105 km. The VTGCM results are summarized in Table 2 along with H12's results.

The overall propagation of the waves in the simulations (#1 and #2) are also lower than what H12 simulated. The Rossby wave only propagates to ~118 km and the Kelvin wave reaches ~125 for simulation #1 and #2 respectively. The H12 results have the Rossby and Kelvin wave propagating up to 130 km. The overall low altitude propagation and the lower maximum amplitude altitude is most likely due to the difference of the wave launching altitude (70 km in the VTGCM versus 80 km in H12) and the atmospheric structure within that region. The VTGCM thermal structure is warmer near the lower boundary and has a slightly stronger vertical thermal gradient than H12; see Figure 3 from this work versus Figure 2 in H12.

3.1.2 Temperature and Zonal Wind Fluctuations - Simulations #3 and #4

A new addition to the VTGCM is the ability to utilize a self-consistent varying (non-uniform) lower boundary from another Venus lower atmosphere GCM. The inclusion of the OXLB changes the atmospheric conditions for launching and propagating the Kelvin and Rossby waves.

The Rossby wave simulation (#3) provided a maximum zonal wind fluctuation of 4.8 m/s at ~91 km and temperature amplitude 3.0 K at ~81 km. The maximum amplitude is higher than both H12 and simulation #1. However, the altitude at which the maximum temperature fluctuation

This article is protected by copyright. All rights reserved.

Author Manuscript

occurs is lower than H12 and simulation #1. The maximum zonal wind fluctuation altitude is higher than simulation #1 but still lower than H12.

The Kelvin wave simulation (#4) utilizes a re-derived geopotential height amplitude, which was discussed in Section 2. The maximum amplitude of the zonal wind velocity fluctuation is approximately 23.4 m/s at ~103 km with a westward phase shift, while the temperature amplitude is 13.8 K at ~92 km. These amplitudes are dramatically higher than Simulation #2 (geopotential height = 110m with a uniform lower boundary) and H12 results. Showing similar behavior as the Rossby wave simulations, the altitude of the maximum temperature amplitude is lower than H12 and simulation #2, while the maximum zonal wind amplitude altitude is higher than simulation #2 but lower than H12. These results from simulation #3 and #4 are summarized in Table 2 in comparison to H12 and the other VTGCM cases.

Overall, the Rossby and Kelvin waves in simulations #3 and #4 propagate up to ~118 km and ~125 km, respectively. These altitudes are lower than the results from H12, where the Rossby and Kelvin wave would propagate up to 130 km. However, these altitudes are similar to simulation #1 and #2.

Table 2 demonstrates the impact the LB has upon Rossby and Kelvin wave propagation. The maximum amplitudes for temperature and zonal winds increased with the OXLB, while the altitude of the maximum amplitudes had opposite trends between the temperature and zonal wind. Temperature maximum amplitudes decreased in altitude while the zonal wind maximum amplitudes increased in altitude. The LB did not impact the overall wave propagation height; these values stayed constant between the simulations. However, these results suggest that both planetary waves strongly depend on the varying cloud top region, which modifies their ability to propagate and the amount of energy deposited into the atmosphere.

This article is protected by copyright. All rights reserved.

Author Manuscript

Author Manuscript

3.2 Kelvin and Rossby Waves Combined Case

The most realistic lower boundary the VTGCM can currently provide is to utilize the OXLB, Rossby waves, and Kelvin waves simultaneously based upon observed temperature and winds near ~70 km. The remainder of the paper will discuss this case of the VTGCM (simulation #5). More specifically, the UMLT (70 – 130 km) region is examined near the equator with a focus on a few atmospheric features along with fluctuations caused by the planetary waves. To help examine this region, the thermal structure, wind structure, CO and O density, and O_2 IR nightglow emission will be analyzed to understand how planetary waves temporally affect these features.

3.2.1 Temperature and Zonal Wind Fluctuations - Simulations #5

Figure 2 demonstrates the fluctuations in temperature and zonal wind due to the combination of Rossby and Kelvin wave propagation from the VTGCM lower boundary near the equator. The maximum amplitude of the temperature fluctuation is 13.3 K near 92 km. The amplitude is much larger than the simulations with just Rossby waves (simulation #3) but about the same as the Kelvin wave, specifically simulation #4. The altitude of the maximum amplitude is higher than simulation #3 and the same as simulation #4. The zonal wind fluctuations produce the same behavior in comparison with the other simulations (#3 and #4). The maximum amplitude from the zonal wind fluctuation is 22.5 m/s at 102 km. These results are summarized in Table 2 with the amplitudes much larger than H12, but the altitudes are slightly lower. The H12 results are replicated in Nakagawa et al. (2013). The overall peak propagation is near 125 km, again lower than H12. These simulations confirm what is expected to be that the Kelvin wave is the more

This article is protected by copyright. All rights reserved.

dominant wave near the equator and that the Rossby wave impacts do not change with the Kelvin wave impacts because of the peak propagation latitude.

3.2.2 Thermal Structure

The planetary waves and OXLB perturbed the thermal structure between 70 km and 110 km, which is demonstrated in Figure 3. The left panels represent the end of a 60 Earth day simulation, while the right panel is the difference between the ending thermal structure and the starting thermal structure for the simulation. From 70 km to 85 km altitude, the temperatures are cooling at all local times. Above ~85 km the atmosphere is heating and cooling dependent on local time and altitude. However, the vertical impact of the planetary waves are minimal above 110 km which is in agreement with Figure 2 and Table 2. Moreover, single local time (LT) profiles for dayside (LT = 12), morning terminator (MT; LT = 06), nightside (LT = 12), and evening terminator (ET; LT = 24) are shown in Figure 4 top left panel for simulation #5. Figure 4 top right panel shows the difference between simulation #5 with waves and without waves (wave minus no wave). It is clearly demonstrated in Figure 4 the impact waves have upon the thermal structure. The dayside has the largest difference in magnitude between the two cases with the temperature ~12 K warmer in the waves case near ~94 km. The ET is also greatly impacted by the waves at ~87 km and ~95 km with +/- 9 K difference. The impact of the waves is seen up to ~120 km for all local times.

3.2.3 Wind Structure

The zonal wind structure largely does not change above ~130 km between the starting history and 60 days after near the equator for simulation #5. The bottom panels of Figure 3 display

This article is protected by copyright. All rights reserved.

Author Manuscript

the resultant zonal wind structure from the 60 day simulation (bottom left) and the difference between the resultant zonal wind structure and the starting zonal wind structure for the simulation (bottom right). Below ~130 km, the waves do perturb the winds structure, as suggested by Figure 2 (right panel) with most of the changes occurring between ~90 km and 110 km. However, simulation #5 does not produce an RSZ flow above ~110 km, as shown in the zonal wind profiles in the bottom left panel of Figure 4. The ET at 120 km is ~20 m/s faster than the MT which is the same as the simulation #5 without waves. The bottom left panel is showing the day, night, MT, and ET vertical profiles at the equator. The bottom right panel of Figure 4 demonstrates the difference between simulation #5 with waves and without waves. The peak difference between the case with and without waves for the MT is at 110 km (+17 m/s difference), for the dayside it is 100 km (+25 m/s difference), the nightside it is near 85 km (+18 m/s difference), and lastly the ET which is near 85 km (-18 m/s difference).

3.2.4 O_2 IR Nightglow

The O_2 IR nightglow emission is an effective tracer of the atmospheric circulation (Bougher et al., 2006; Gérard et al., 2017). The chemical sources of O_2 IR nightglow emission (atomic O) are created on the dayside and are transported to the nightside where three-body recombination takes place. The strength and altitude variation of the winds controls the intensity of the emission. With the current simulation inputs and the parameters set as in Brecht and Bougher (2012), the O_2 IR volume emission rate (VER) is 2.13 x 10^6 photons cm^3 s^{-1} at 100 km at midnight. The four panels of Figure 5 represent different slices of the simulated O_2 IR nightglow emission from the end of simulation #5. The top left panel of Figure 5 is a latitude versus local time map showing the peak horizontal location. The top right panel shows altitude versus log

This article is protected by copyright. All rights reserved.

Author Manuscript

emission rate to demonstrate the vertical extent of the emission. The bottom two panels represent the VER at the equator (left) and at midnight (right). The peak VER is relatively broad with respect to latitude and local time. The peak integrated vertical intensity is 1.4 MR (R = Rayleigh = 10^6 photons cm^{-2} s^{-1} into 4π sr), which is close to the statistical peak intensity observed by VEX VIRTIS (1.6 MR) (Soret et al., 2012).

3.2.5 Atmospheric Composition – CO_2, O, CO

Figure 6 shows the CO_2 density profile for a latitude bin of 0° – 30° at day time (LT=12) and night time (LT=00). At 70 km, the density does not vary with local time. Around 110 km the density profiles start to diverge (mixing ratio strongly diverges above ~130 km). The VTGCM CO_2 density profiles compare reasonably with Limaye et al. (2017) Figure 20, where multiple VEX instrument observations have been combined for comparison. Figure 6 left panel represents CO_2 as number density and has the night time profiles from VEX SPICAV and VeRa observations (Bertaux et al., 2007; Piccialli et al., 2015; Tellmann et al., 2012). The VTGCM night time profile is larger than the observed SPICAV above ~100 km by ~5% near 1 x 10^{-4} mbar.

The O and CO density profiles are shown in Figure 7, where the vertical region spans the area most impacted by the planetary waves (70 km to 130 km). The top left panel is atomic oxygen number density at the equator for specific LT (06, 12, 18, 00/24). The top right panel is carbon monoxide number density for a latitude bin 10S – 10N and four LT bins (04-08, 10-14, 16-20, 02-22). This was done to be consistent with observations shown in those panels. The bottom two panels show the chemical species as mass mixing ratio and volume mixing ratio, respectively. All four panels have profiles to represent simulation #5 with waves.

This article is protected by copyright. All rights reserved.

Author Manuscript

The maximum density of atomic oxygen for LT = 12 is 8.3 x 10^{10} cm^{-3} at ~93 km, while the maximum density for LT=00 is 5.8 x 10^{11} cm^{-3} at 100 km. These maximum values are higher than past simulations (Brecht et al., 2011; Brecht et al., 2012) due to neglecting the additional asymmetric Rayleigh friction to force an RSZ wind above ~110 km, which in turn modifies the transport toward the nightside. The nightside density steeply drops off below 100 km until about ~87 km. This is due to prescribed trace chemical species on the nightside regulating atomic oxygen and the newly implemented sulfur chemistry (Brecht et al., 2011; Parkinson et al., 2019). The terminator profiles peak at similar altitudes and have similar profile shapes. There is very minimal difference between simulation #5 with waves and without waves for atomic oxygen. The percent difference of the log density is less than a percent, except for all local times near 90 km it is ~1%.

Carbon monoxide profiles for the dayside and nightside LT bins have a small "bulge" near the same peak altitude as the atomic oxygen. At dayside (LT = 10-14) the slight "bulge" is near 96 km with a value of 2.2 x 10^{11} cm^{-3}, while the nightside (LT = 2-22) has a more defined "bulge" at 96 km with a density of 8.2 x 10^{11} cm^{-3}. The nightside profile also shows a defined lower peak with a maximum density of is 1.2 x 10^{13} cm^{-3} at ~83 km. The overall nightside profile is larger than other local times from ~80 km to ~120 km, which is due to the strong day-to-night zonal circulation. The evening terminator profile and the morning terminator profiles have lower peaks at different vertical locations, ~90 km and ~80 km respectively, but are similar magnitudes between ~100 km and ~120 km. The 10 km difference between these peak CO densities is unexpected and demonstrates the CO density is sensitive to the planetary waves. Furthermore, as it is with the atomic oxygen, CO has minimal variation between simulation #5 with and without waves. The maximum variation was near 90 km for all LT, with 7% being the largest log density percent difference for the ET (LT=16-20). This is due to the wave propagation going westward.

This article is protected by copyright. All rights reserved.

Author Manuscript

The westward propagation is in the same direction as the planet solid-body rotation and cloud top winds. Wave damping would be minimal on the ET due to same direction (less critical layers) while the MT has opposing wind direction to cloud top winds which creates damping (more critical layers).

4 Discussion

4.1 Comparisons of Simulation #5 with Observations – T, O, CO

The thermal structure is not only sensitive to radiative affects, but also dynamical. The current understanding of the Venusian thermal structure from observations is discussed in Limaye et al. (2017), where details of the upcoming discussion about observations and binning can be found. Simulated thermal structure changes in response to the planetary waves are shown in Figure 8 and 9. Figure 8 compares the VTGCM simulation variation with some of the datasets discussed within Limaye et al. (2017), while Figure 9 demonstrates the percent relative difference within the last four days of simulation. Model versus observations comparisons are made with ground based Heinrich Hertz Submillimeter Telescope (HHSMT) (Rengel et al., 2008), ground based James Clark Maxwell Telescope (JCMT) (Clancy et al., 2012b), Heterodyne Instrument for Planetary Wind and Composition (HIPWAC-THIS) (Kostiuk et al., 2006; Kostiuk & Mumma, 1983; Sonnabend et al., 2010; Sornig et al., 2008, 2012), VEX instrument Visible and InfraRed Thermal Imaging Spectrometer H and M channels (VIRTIS-H and VIRTIS-M) (Arnold et al., 2012; Garate-Lopez et al., 2015; Gilli et al., 2015; Grassi et al., 2008, 2010, 2014; Haus et al., 2014; Migliorini et al., 2012),VEX Radio Science Experiment (VeRa) (Häusler et al., 2006, 2007), VEX instrument Solar Occultation Infrared (SOIR) (Mahieux et al., 2008, 2012, 2015a, 2015b;

This article is protected by copyright. All rights reserved.

Author Manuscript

Vandaele et al., 2013), and VEX instrument Spectroscopy for Investigation of Characteristics of the Atmosphere of Venus (SPICAV) (Bertaux et al., 2007; Piccialli et al., 2015).

The VTGCM is able to reproduce the general observed profile trends for the three LT presented in Figure 8. The solid lines represent the mean of the last four days of the simulation or the actual observation. The shadowing represents the minimum value and maximum value during the last four days of the simulation or the variation/error bars of the observations. The top panel is nightside, the middle panel is both morning and evening terminators, and the bottom panel is dayside.

Day Temperatures: There are a minimal number of datasets for the dayside of Venus and a few of those datasets are presented in Figure 8 (bottom panel) with the VTGCM simulation #5. Below 90 km the VTGCM is colder than both HHSMT and VeRa. The VeRa observations do have a ~40 K temperature variation near 90km and the VTGCM simulation is within the lower end of the range but only has ~15 K temperature variation (see Figure 9, top left panel). However, the VTGCM is in great agreement with the HHSMT between ~90 km and ~105 km. Above ~105 km the VTGCM is much warmer than the observations from the VIRTIS-H and HHSMT, though within the very large error bars of VIRTIS-H and HIPWAC-THIS.

Terminator Temperatures: The largest dataset at the terminators is from SOIR. Previous VTGCM simulations have been compared to SOIR in detail by Bougher et al. (2015) and the current simulation compared to the profiles in Limaye et al. (2017) produce similar results (Figure 8 middle panel). The SOIR observations are mostly warmer than the VTGCM simulation. The VeRa observations are warmer too but the VTGCM simulation overlaps VeRa's observed variation around 90km. The VeRa observations have ~50 K temperature variation at 90 km, while SOIR temperatures vary ~30 K and ~50 K for the MT and ET respectively. The planetary waves

This article is protected by copyright. All rights reserved.

Author Manuscript

within the simulation do not provide as large of variations as seen in the observations. This could be due to other missing wave mechanisms (e.g. gravity waves) and not properly accounting for a combination of source variability, background state variability, and interaction among various wave components. At 90 km the simulation produces ~8 K and ~15 K temperature variation for the MT and ET respectively. However, the simulation is consistent with the observed ET having larger variations than the MT. This is also shown in Figure 9, top left panel, where the ET percent relative difference change peaks ~10% at ~90 km and the MT is about half the difference at 90 km.

Night Temperatures: The nightside thermal structure of the Venusian UMLT was thought to be most dominated by radiative cooling and was considered a "cryosphere". However, VEX observations began augmenting this notion with the SPICAV instrument observing a warm layer at ~100 km (Bertaux et al., 2007); shown in Figure 8, top panel. In other observations, HHSMT shown in Figure 8 top panel, have also observed a warm layer around 100 km but the average magnitude is not consistent across the different observations (Bailey et al., 2008a; Clancy et al., 2008; Rengel et al., 2008). Brecht et al. (2011) determined through VTGCM simulations the nightside warm layer was due to the adiabatic heating from the enhanced day-to-night winds driven by the 4.3 μm heating on the dayside. The nightside warm layer continues to be reproduced within the VTGCM with a peak temperature of 195 K at 100 km. Previous VTGCM simulation in Brecht et al. (2011) had a warm layer peak of 188 K at 103 km. These values, temperature and altitude, are within the observational range summarized in Brecht et al. (2011) Table 5. Moreover, the peak can be directly compared to HHSMT and SPICAV observations in Figure 8. As with the dayside, the VTGCM simulation and HHSMT observations are in good agreement between ~90 km and ~110 km. The SPICAV observations are warmer and lower in altitude (peak mean temperatures

This article is protected by copyright. All rights reserved.

Author Manuscript

are ~215 K and 209 K at ~0.2 mbar (~90 km)) compared to the simulation. Above ~110 km, the simulation is cooler than SPICAV but within the observational variation. In addition, the simulation is cooler than the HHSMT observations, but warmer than JCMT observations above ~110 km. Below 90 km, the simulation is 20 – 50 K cooler than the observations but overlaps the VeRa observed variation at ~90 km. The cooler simulation temperatures below ~85 km are thought to be due to missing radiative effects from aerosols (see Gilli et al., 2015).

O_2 IR nightglow: The O_2 IR nightglow emission has been observed by ground based telescopes (Allen et al., 1992; Bailey et al., 2008b; Connes et al., 1979; Crisp, 1996; Ohtsuki et al., 2005, 2008), but the VEX VIRTIS has provided the most comprehensive dataset (e.g. Drossart et al., 2007; Gérard et al., 2008; Piccioni et al., 2009). Soret et al. (2012) created the most complete statistical emission map of the O_2 IR nightglow from the available nadir and limb observations. The statistical peak intensity observed by VIRTIS was 1.6 MR, which is stronger than the VTGCM simulation mean (1.4 MR). However, the current peak integrated intensity and VER are comparable to the results in Brecht et al. (2011), and the differences are largely due to the zonal wind. The VTGCM peak altitude is 3 km higher than the statistically observed average of 97 km.

O and CO: The atomic oxygen density was largely discussed and compared to observations in Brecht et al., 2011 and Brecht et al., 2012. The current simulated maximum density of atomic oxygen for LT = 12 is 8.3 x 10^{10} cm^{-3} at ~93 km, while the maximum density for LT=00 is 5.8 x 10^{11} cm^{-3} at 100 km. The dayside peak altitude is about the same as previous simulations (94 km) but the current magnitude is larger (by ~50%). The current nightside peak is 4 km lower with a larger magnitude (by ~70%). These differences are due to the different wind structure produced by the planetary waves and the removal of asymmetrical Rayleigh friction. Figure 7, top left, displays the VTGCM atomic oxygen profiles at different local times and it also shows the derived

This article is protected by copyright. All rights reserved.

Author Manuscript

atomic oxygen profile from the VEX instrument VIRTIS (Soret et al., 2012). Atomic oxygen density was derived from O_2 IR nightglow statistical maps from VEX nadir and limb observations with the VIRTIS instrument (Gérard et al., 2008; Piccioni et al., 2009). The simulation peaks at a near the same altitude and has a larger magnitude then the observationally derived profile (2.86 x 10^{11} cm^{-3} at 102 km). The simulation does have a larger drop off below the peak compared to the VIRTIS profile. This suggests a need for a more detailed look at the sulfur chemistry and trace chemical species because the chemical timescales at these altitudes become competitive or shorter than the dynamics timescales. However, the VTGCM is still within the observations range, which was deduced to be between 1 x 10^{11} and 5 x 10^{11} cm^{-3} at 95 to 115 km range by Gérard et al. (2009). Along with the observed range, the derivation technique error is ~30% (see Gérard et al., 2009 for more details).

The CO VMR day and night profiles are compared with ground based observations in Figure 7, bottom right panel. Clancy et al. (2012a) conducted two ground based observing campaigns; one from 2007-2009 and another from 2000-2002. Both produced disk averaged day and nightside profiles. They found two distinctions between the observation's periods: (1) the 2007-2009 VMR observations were a factor-of-two lower than the 2000-2002 observations and (2) VMR diurnal variations in the lower thermosphere were roughly half as large in the 2007-2009 versus the 2000-2002 observations. Lellouch et al. (1994) had a 6-day observing period in August of 1991 where the majority of the observations were on the nightside (LT range of 17.3 to 5.3), however Figure 7 shows only two beam positions representing LT = 23 at latitude 8° and LT = 22 at latitude -10°. The nightside VTGCM results fit within the range of ground based observations, while the dayside VTGCM profile is less then observed below 95 km. The decrease on the dayside below 95 km and the increase on the nightside below 95 km is connected to the strength of the

This article is protected by copyright. All rights reserved.

Author Manuscript

zonal wind and the effects of trace species chemistry. The trace species chemistry has only been included on the nightside for O and CO as prescribed profiles from the 1-D KINETICS model (Brecht et al., 2011). VEX has made CO observations that have been discussed in Gilli et al. (2015) and Vandaele et al. (2015). Figure 7 (top right) shows the VIRTIS-H CO observations for their box of Latitude = 10S to 10N and LT = 10-14. The VTGCM dayside profile is less then observed by VIRTIS-H, which is thought to be caused by the cooler temperatures between 70-95 km. However, the VIRTIS-H observations showed a gradient from dayside to the terminators at the equator of a factor ~2. While the VTGCM gradient from dayside to the terminators is less, the day to night gradient can be as large as an order of magnitude. A detailed data-model comparison has been discussed in detail within Gilli et al. (2015). Gilli et al. (2017) presents overall results from their full atmosphere Venus GCM (Laboratoire de Météorologie Dynamique (LMD)), but plots from 90 km to 150 km. The LMD-VGCM and VTGCM are in reasonable agreement based on the vertical variation trend and magnitude. However, their night time bulge is slightly larger and seems more pronounced then the VTGCM, but the figure cuts off at 90 km. Vandaele et al. (2015) focused only on observations near the pole, but did determine CO densities and VMR have high variability on relatively short-term periods (days to months). Vandaele et al. (2016) extended their previous work with more observations and provided an update to a Venus empirical model with the VEX SOIR observations. The SOIR observed only on the terminators, thus the profiles are at LT=6 and LT=18. For a latitude bin of 0 to 30, the profiles start ~70 - 80 km and reach up to ~135 - 140 km. Vandaele et al. (2016) found the MT to have larger values than the ET below 105 km while the trend reversed above 105 km. The VTGCM results in Figure 7 demonstrate the MT being larger than the ET from ~75 – ~87 km and above they terminators have similar values. Again, this is due to the minimal zonal wind difference at the higher altitudes in the current model.

This article is protected by copyright. All rights reserved.

Author Manuscript

However, the SOIR observations show vertical variability that is similar to the VTGCM lower peak and "bulge". For the MT the lower peak ranges between 80 and 85 km while the "bulge" is near 105 km. The ET lower peak ranges from 90 – 100 km and the "bulge" is near ~115 km. The VTGCM results are in line with these observations (Figure 7).

The CO latitude variation within the VTGCM simulation is largest at LT=02-22 (NT) from 80 km to 115 km, where it changes by a factor of 3.5 near 100 km. This is shown in Figure 10. The left four panels show CO VMR versus simulation time (last 10 days of simulation #5) at four different altitudes and the right panel demonstrates the vertical profiles of CO density for the last time of simulation #5. The NT latitude variation is produced without planetary waves and OXLB but the planetary waves create the slight depression ~93 km and slight bulge ~97 km. This is due to the day to night zonal winds and the Rayleigh friction cos(lat) dependence. The LT=16-20 (ET) has a smaller altitude range where CO varies latitudinal around a factor of 2 near 95 km. The planetary waves enhance the ET latitude variation near 95 km but the dynamical response to the OXLB produces the minimum near 81 km. The LT=10-14 (DT) and LT=04-08 (MT) latitude variations are due to dynamical response to OXLB and demonstrate minimal changes from the planetary waves (< factor of 2). The time series panels of Figure 10 clearly show wave structure which is driven by the planetary waves. The planetary waves do provide a small increase (~factor of 2) in latitudinal variation for the DT, MT, and ET compared to no planetary waves. These results are in line with VIRTIS-H observations that extend from ~105 km to 145 km (Gilli et al., 2015). The equatorial values were found to be a factor of 2 larger than the high latitudes around mid-day. This latitude trend was observed at the MT and ET but with a smaller gradient. Vandaele et al. (2016) were able to perform a latitude study based on their SOIR CO observations. They noticed a general trend of CO decreasing from the equator to the pole above 100 km (factor of 2 -

This article is protected by copyright. All rights reserved.

Author Manuscript

4 difference ~130 km), while below 100 km the trend is reversed and weaker. The VTGCM simulation only slightly replicates this trend for the NT but the cross over altitude is near 120 km. Again, the influence of the planetary waves is seen below ~110 km, suggesting observed variations above ~110 km are due to smaller scale waves. A more detailed study needs to be conducted between the VTGCM simulations and observations, but is currently beyond the scope of this work.

To help understand the behavior of O and CO, assessing the timescales of dynamics, mixing, and chemistry are shown in Figure 11. This shows the time scales of the chemistry, eddy mixing, and dynamics for four LT locations (06, 12, 18, 24) near the equator. The chemical lifetime is calculated as the inverse of the loss frequency with O or CO being the chemical species of concern. Eddy diffusion lifetime is estimated by $\tau_{eddy} = H^2/K_{eddy}$, where H is the mean scale height (H=RT/mg, where R is the universal gas constant, T is neutral temperature, m is mean molecular weight, g is gravity). And K_{eddy} is the eddy diffusion coefficient. The lifetime corresponding to the horizontal wind (motion of a parcel of air) utilizes the wind velocity of the specific LT, where $\tau_{horizontal} = \frac{\pi(Rv+Z)}{Un}$. Rv is Venus radius (6.052 x 10^8 cm), Z is altitude, and Un is the zonal wind at a specific LT. It should be noted that the horizontal velocity at LT = 12 and 24 is very small (and dynamical timescales long), since these are the symmetric circulation divergence and convergence points, respectively. Therefore, the LT=12 panel does not show a horizontal wind lifetime and at LT = 24 the horizontal wind is represented by the horizontal wind at LT=18, as has been done in previous work. The vertical wind lifetime is $\tau_{vertical} = H/\omega$, where ω vertical motion is in units of cm/sec.

It is clear the chemical lifetime of atomic oxygen is much shorter than the dynamics (<100 km) at all LT locations, thus changes within atomic oxygen are driven by chemistry and not the dynamics. Above 100 km, atomic oxygen is controlled by dynamics. This was shown in Brecht

This article is protected by copyright. All rights reserved.

Author Manuscript

et al. (2011). For carbon monoxide, its chemical lifetime is only competitive with the dynamics on the nightside (at LT=24) below 80 km and at other times it is greatly longer than the dynamics (LT=06, 12, 18). Therefore, CO is mainly driven by the dynamics. It is noteworthy that the 3-body reaction (CO+O+M), is a major loss mechanism for CO near ~100 km nightside altitudes, and HOx and ClOx species seem to control the chemical timescale for CO below 100 km, in part due to the declining abundance of oxygen at these same altitudes. These timescales explain why O does not demonstrate as large of variation as CO below ~90 km (see Figure 9). The planetary waves are most dominant below 100 km, where O is controlled by chemistry and CO is mostly controlled by dynamics (i.e. influenced by waves).

4.2 Temporal Variation

From the results section, it has been shown that planetary waves change the upper mesosphere structure (<110 km) substantially when comparing the start and end of a 60-day simulation (this paper) and from previous simulations (Brecht et al., 2011). For temporal variation (such as day to day), Figure 9 has four panels showing the percent relative difference of change in temperature, zonal wind, atomic oxygen, and carbon monoxide to demonstrate temporal variation over 4 Earth days. The percent relative difference of change is calculated by: $\left(\frac{|max\ value - min\ value|}{|max\ value + min\ value|/2}\right) * 100$. The maximum value and minimum value are over the last 4 Earth days of the 60-day simulation at each altitude. The profiles represent a specific time of day (daytime, nighttime, ET, and MT) averaged over 0° to 30° latitude to be consistent with Figure 8 and observations.

The thermal profiles are largely changing between 80 km and 110km altitude range which is consistent with the thermal fluctuations in Figure 2. At all local times, the effects of the waves are gone above 120 km. The waves seem to propagate the most in the evening terminator and

This article is protected by copyright. All rights reserved.

Author Manuscript

daytime, with the highest altitudes during the day. The dayside has the largest change with 14% near 98 km, with the ET being the second largest at ~11% near 90km. This suggests the planetary waves are propagating to higher altitudes on the dayside and creating dynamical feedbacks to the thermal structure. The temperature variation within the simulation is small compared to most observations. By examining the observations in Figure 8, along with Figure 15 in Limaye et al. (2017), the dayside observations suggest ~40 K change near 85 km, ~10-15 K change near 90 km, and ~100 K change near 110 km. The observed evening terminator has even larger variations, especially by the VEX SOIR instrument. SOIR observations are warmer at the ET than the other observations by ~50 K near 85 km. Though, SOIR suggests a variation of around 20 K near 85 km, while the other observations produce approximately 40 K variation near 85 km. Near 105 km, SOIR has observed ~100 K change while the other observations suggest ~10 K. Planetary waves do provide substantial variation within the VTGCM; however, it seems not to be as large a source as has been observed in SOIR datasets.

The planetary waves affect the zonal wind profiles from 75 km to ~130 km (Figure 9, top right). All four local times show large variations. Between 80 km and 90 km; the dayside, nightside, and MT vary the most. While between 90 km and ~100 km, ET have the largest variation. This is consistent with the location of fluctuations as shown in Figure 2.

The atomic oxygen profiles vary the most between 90 km and 100 km, with the largest variation on the nightside and ET (Figure 9, bottom left). The atomic oxygen peak at 90 km changes ~8% at night time and ~7% at ET. This is in agreement with the largest zonal wind variation near 90 km, which is also the nightside and ET. Moreover, this is near the O timescale boundary of when chemistry and dynamics are competing. Carbon monoxide, however, has significant variation between ~80 km and 100 km only on the ET (Figure 9, bottom right). There

This article is protected by copyright. All rights reserved.

Author Manuscript

are small variations (<4%) in carbon monoxide on the nightside, dayside, and MT between ~80 km and 100 km. This is due to the direction of the propagating waves (westward).

Figure 12 demonstrates how the nightglow emission can vary within many Earth days. The left panel is a series of vertical profiles of the peak O_2 IR nightglow VER. The colors represent every 6 hours over the last 4 Earth days of simulation #5. It shows the peak altitude changing 2 km over the 4 days and the magnitude of the intensity varies ~30% near 98 km. This behavior again shows the planetary wave impact is stronger below 100 km. The peak emission varies between 2 x 10^6 photons cm^3 s^{-1} and 2.6 x 10^6 photons cm^{-3} s^{-1}. Figure 12 (top right panel) shows the O_2 IR integrated intensity variation for the last 20 Earth days of the simulations. The green line is simulation #5 without planetary waves and the black line represents the simulation with the planetary waves. The variation in the green line is due to the OXLB. The simulation has nearly a 4-day periodicity. The OXLB and Rossby wave alters the variation minimally compared to the Kelvin wave. The intensity does vary between 1.2 MR to 1.65 MR. The intensity range is wider than what was presented in H12 (1.11 MR to 1.32 MR), however it is similar to the VIRTIS observations shown in Soret et al. (2012). The VIRTIS observations show a range from ~0.79 MR to 1.58 MR. The reason simulation #5 has a wider range than H12 is because of the OXLB. In comparison to simulation #2 (uniform LB with Kelvin waves), the VTGCM reproduces a similar intensity range as H12. The bottom right panel of Figure 12 is the LT variation over 20 Earth days. The planetary waves vary the LT between ~0.33 LT to ~23 LT. This variation is slightly larger than H12 results, but Soret et al. (2012) statistically shows the LT variation to be wider (~0h1 - ~23h).

This article is protected by copyright. All rights reserved.

Author Manuscript

Author Manuscript

5 Conclusions

In this paper it has been demonstrated that including planetary waves (Kelvin and Rossby waves) within the VTGCM provides variability within the UMLT of Venus. The thermal structure and zonal winds largely do not change above ~120 km, though below ~120 km the Kelvin wave is the dominant source of variation. This is in line with previous modeling work by H12. Moreover, the VTGCM simulations were able to replicate the thermal and zonal wind fluctuations presented in H12. The model improvement in this paper is the additional inclusion of a varying lower boundary (OXLB). The OXLB is from a lower atmosphere GCM and consists of temperature, zonal wind, meridional wind, and geopotential height fields at a constant pressure (44.4 mbar), which provides a pseudo connection to the lower atmosphere. The OXLB creates a favorable environment to launch waves and increases the wave strength but not propagation height. Temperature and zonal wind fluctuations in simulation #5 are higher than H12 but the impacting altitude is lower than H12, which could be due to different background atmospheres (thermal and zonal wind structure). Temperature fluctuations due to Kelvin waves within the VTGCM were ~13 K versus 2.5 K in H12. The thermal variation from simulation #5 did not fully reproduce observed variations. This suggests the model is missing other wave mechanisms and not fully capturing interaction between various wave components and the varying background state. Zonal wind fluctuations due to Kelvin waves within the VTGCM are ~23 m/s versus 6 m/s in H12. However, having Kelvin and Rossby waves with the OXLB do not produce a strong retrograde wind in the VTGCM simulations.

The atmospheric composition also varies due to the planetary waves, but most strongly CO (~12% relative difference over 4 Earth days on the ET). The CO variation is comparable to SOIR observations (Vandaele et al., 2016). The simulated O_2 IR nightglow emission integrated intensity

This article is protected by copyright. All rights reserved.

varies with a ~4-day period from 1.2 MR to 1.65 MR. The intensity range is very similar to VEX observations (0.8 MR to 1.6 MR). The local time of the peak intensity has a small variation, while there is no variation in latitude. The lack of spatial variation is most likely due to the nightglow concentration near the equator and VTGCM model resolution. Atomic oxygen and carbon monoxide both demonstrated variations caused by planetary waves, but these are confined to a small altitude range (80 km – 100 km). The favorable local time for the chemical variation is mainly the ET.

The role of planetary waves in the Venusian UMLT is important to understand, but planetary waves are only one piece of the puzzle. It is also important to examine waves that do propagate from below the clouds up to thermospheric altitudes (unresolved variations). The planetary waves do affect the atmospheric structure but there are still observed large variations the planetary waves cannot explain (i.e. thermal structure). A few VTGCM model improvements that need to be addressed to help further advance the investigation of variability in Venus' atmosphere include: (1) increasing model resolution (horizontal and vertical), (2) lowering the model lower boundary altitude, (3) examining the more complex atmospheric variations due to small-scale waves (i.e. gravity waves) combined with planetary waves, and (4) the inclusion of aerosol radiative feedbacks, particularly below ~85 km.

Acknowledgments

This research was supported by the NASA ROSES Solar System Workings program. The authors would like to thank the reviewers' extensive comments that helped shape this paper. The temperature data in Figure 8 was graciously provided by S. Limaye and S. Lebonnois. This research benefited from discussions with R. J. Wilson. Resources supporting this research were

This article is protected by copyright. All rights reserved.

Author Manuscript

provided by the NASA High-End Computing (HEC) Program through the NASA Advanced Supercomputing (NAS) Division at Ames Research Center. The VTGCM simulations are available at the Deep Blue Data repository at the University of Michigan Library (Bougher and Brecht, 2020).

References

Allen, D., Crisp, D., & Meadows, V. S. (1992). Variable oxygen airglow on Venus as a probe of atmospheric dynamics. *Nature*, *359*(6395), 516–519. https://doi.org/10.1038/359516a0

Altieri, F., Migliorini, A., Zasova, L., Shakun, A., Piccioni, G., & Bellucci, G. (2014). Modeling VIRTIS/VEX O 2 (a 1Δ g) nightglow profiles affected by the propagation of gravity waves in the Venus upper mesosphere. *Journal of Geophysical Research: Planets*, *119*(11), 2300–2316. https://doi.org/10.1002/2013JE004585

Arnold, G. E., Haus, R., Kappel, D., Piccioni, G., & Drossart, P. (2012). VIRTIS/VEX observations of Venus: overview of selected scientific results. *Journal of Applied Remote Sensing*, *6*(1), 063580–063581. https://doi.org/10.1117/1.JRS.6.063580

Bailey, J., Chamberlain, S., Crisp, D., & Meadows, V. S. (2008a). Near infrared imaging spectroscopy of Venus with the Anglo-Australian Telescope. *Planetary and Space Science*, *56*(10), 1385–1390. https://doi.org/10.1016/j.pss.2008.03.006

Bailey, J., Meadows, V. S., Chamberlain, S., & Crisp, D. (2008b). The temperature of the Venus mesosphere from O2 (a 1Δg) airglow observations. *Icarus*, *197*(1), 247–259. https://doi.org/10.1016/j.icarus.2008.04.007

This article is protected by copyright. All rights reserved.

Author Manuscript

Author Manuscript

Belton, M. J. S., Smith, G. R., Schubert, G., & Del Genio, A. D. (1976). Cloud Patterns, Waves and Convection in the Venus Atmosphere. *Journal of the Atmospheric Sciences*, *33*(8), 1394–1417. https://doi.org/10.1175/1520-0469(1976)033<1394:CPWACI>2.0.CO;2

Bertaux, J. L., Khatuntsev, I. V., Hauchecorne, A., Markiewicz, W. J., Marcq, E., Lebonnois, S., Patsaeva, M., Turin, A., & Fedorova, A. (2016). Influence of Venus topography on the zonal wind and UV albedo at cloud top level: The role of stationary gravity waves. *Journal of Geophysical Research: Planets*, *121*(6), 1087–1101. https://doi.org/10.1002/2015JE004958

Bertaux, J. L., Nevejans, D., Korablev, O., Villard, E., Quémerais, E., Neefs, E., Montmessin, F., Leblanc, F., Dubois, J. P., Dimarellis, E., Hauchecorne, A., Lefèvre, F., Rannou, P., Chaufray, J. Y., Cabane, M., Cernogora, G., Souchon, G., Semelin, F., Reberac, A., … Gérard, J. C. (2007). SPICAV on Venus Express: Three spectrometers to study the global structure and composition of the Venus atmosphere. *Planetary and Space Science*, *55*(12), 1673–1700. https://doi.org/10.1016/j.pss.2007.01.016

Bougher, S. W., & Borucki, W. J. (1994). Venus O 2 visible and IR nightglow: Implications for lower thermosphere dynamics and chemistry . *Journal of Geophysical Research*, *99*(E2), 3759. https://doi.org/10.1029/93je03431

Bougher, S. W., Brecht, A. S. (2020). Planetary-scale Wave Impacts on the Venusian Upper Mesosphere and Lower Thermosphere: Supporting Datasets for VTGCM Numerical Simulations. University of Michigan - Deep Blue. https://doi.org/10.7302/6jz8-7195

Bougher, S. W., Brecht, A. S., Schulte, R., Fischer, J., Parkinson, C. D., Mahieux, A., Wilquet, V., & Vandaele, A. (2015). Upper atmosphere temperature structure at the Venusian

This article is protected by copyright. All rights reserved.

terminators: A comparison of SOIR and VTGCM results. *Planetary and Space Science*, *113–114*, 336–346. https://doi.org/10.1016/j.pss.2015.01.012

Bougher, S. W., Dickinson, R. E., Ridley, E. C., & Roble, R. G. (1988). Venus mesosphere and thermosphere. *Icarus*, *73*(3), 545–573. https://doi.org/10.1016/0019-1035(88)90064-4

Bougher, S. W., Gérard, J. C., Stewart, A. I. F., & Fesen, C. G. (1990). The Venus nitric oxide night airglow: Model calculations based on the Venus thermospheric general circulation model. *Journal of Geophysical Research*, *95*(A5), 6271. https://doi.org/10.1029/ja095ia05p06271

Bougher, S. W., Rafkin, S., & Drossart, P. (2006). Dynamics of the Venus upper atmosphere: Outstanding problems and new constraints expected from Venus Express. *Planetary and Space Science*, *54*(13–14), 1371–1380. https://doi.org/10.1016/j.pss.2006.04.023

Brecht, A. S. (2011). *Tracing the Dynamics in Venus ' Upper Atmosphere.* PhD thesis, Univ. of Michigan, Ann Arbor.

Brecht, A. S., & Bougher, S. W. (2012). Dayside thermal structure of Venus' upper atmosphere characterized by a global model. *Journal of Geophysical Research E: Planets*, *117*(8), 1–10. https://doi.org/10.1029/2012JE004079

Brecht, A. S., Bougher, S. W., Gérard, J. C., Parkinson, C. D., Rafkin, S., & Foster, B. (2011). Understanding the variability of nightside temperatures, NO UV and O 2 IR nightglow emissions in the Venus upper atmosphere. *Journal of Geophysical Research E: Planets*, *116*(8), 1–25. https://doi.org/10.1029/2010JE003770

Brecht, A. S., Bougher, S. W., Gérard, J. C., & Soret, L. (2012). Atomic oxygen distributions in the Venus thermosphere: Comparisons between Venus Express observations and global

This article is protected by copyright. All rights reserved.

Author Manuscript

model simulations. *Icarus*, *217*(2), 759–766. https://doi.org/10.1016/j.icarus.2011.06.033

Brecht, A. S., Bougher, S. W., Yi, E., & Liu, H. (2019). Understanding the impact of waves on Venus ' Upper Atmosphere through General Circulation Model Simulations. *International Venus Conference*, Niseko, Hokkaido, Japan.

Clancy, R. T., Sandor, B. J., & Moriarty-Schieven, G. (2012a). Circulation of the Venus upper mesosphere/lower thermosphere: Doppler wind measurements from 2001-2009 inferior conjunction, sub-millimeter CO absorption line observations. *Icarus*, *217*(2), 794–812. https://doi.org/10.1016/j.icarus.2011.05.021

Clancy, R. T., Sandor, B. J., & Moriarty-Schieven, G. (2012b). Thermal structure and CO distribution for the Venus mesosphere/lower thermosphere: 2001-2009 inferior conjunction sub-millimeter CO absorption line observations. *Icarus*, *217*(2), 779–793. https://doi.org/10.1016/j.icarus.2011.05.032

Clancy, R. T., Sandor, B. J., & Moriarty-Schieven, G. H. (2008). Venus upper atmospheric CO, temperature, and winds across the afternoon/evening terminator from June 2007 JCMT sub-millimeter line observations. *Planetary and Space Science*, *56*(10), 1344–1354. https://doi.org/10.1016/j.pss.2008.05.007

Connes, P., Noxon, J. F., Traub, W. A., & Carleton, N. P. (1979). O2/1 Delta/ emission in the day and night airglow of Venus. *The Astrophysical Journal*, *233*, L29. https://doi.org/10.1086/183070

Counselman, C. C., Gourevitch, S. A., King, R. W., Loriot, G. B., & Ginsberg, E. S. (1980). Zonal and meridional circulation of the lower atmosphere of Venus determined by radio interferometry. *Journal of Geophysical Research*, *85*(A13), 8026.

This article is protected by copyright. All rights reserved.

Author Manuscript

https://doi.org/10.1029/ja085ia13p08026

Crisp, D. (1986). Radiative forcing of the Venus mesosphere. I. Solar fluxes and heating rates. *Icarus*, *67*(3), 484–514. https://doi.org/10.1016/0019-1035(86)90126-0

Crisp, D. (1996). Ground-based near-infrared observations of the Venus nightside: 1.27-μm O2(a1 Δg) airglow from the upper atmosphere. In *Journal of Geophysical Research E: Planets* (Vol. 101, Issue E2, pp. 4577–4593). https://doi.org/10.1029/95JE03136

Del Genio, A. D., & Rossow, W. B. (1990). Planetary-scale waves and the cyclic nature of cloud top dynamics on Venus. In *Journal of the Atmospheric Sciences* (Vol. 47, Issue 3, pp. 293–318). https://doi.org/10.1175/1520-0469(1990)047<0293:PSWATC>2.0.CO;2

Dickinson, R. E., Ridley, E. C., & Roble, R. G. (1981). A three-dimensional general circulation model of the thermosphere. *Journal of Geophysical Research*, *86*(A3), 1499. https://doi.org/10.1029/ja086ia03p01499

Drossart, P., Piccioni, G., Gérard, J. C., Lopez-Valverde, M. A., Sanchez-Lavega, A., Zasova, L., Hueso, R., Taylor, F. W., Bézard, B., Adriani, A., Angrilli, F., Arnold, G., Baines, K. H., Bellucci, G., Benkhoff, J., Bibring, J. P., Blanco, A., Blecka, M. I., Carlson, R. W., … Ulmer, B. (2007). A dynamic upper atmosphere of Venus as revealed by VIRTIS on Venus Express. *Nature*, *450*(7170), 641–645. https://doi.org/10.1038/nature06140

Fox, J. L., & Sung, K. Y. (2001). Solar activity variations of the Venus thermosphere/ionosphere. *Journal of Geophysical Research: Space Physics*, *106*(A10), 21305–21335. https://doi.org/10.1029/2001ja000069

Fukuhara, T., Taguchi, M., Imamura, T., Hayashitani, A., Yamada, T., Futaguchi, M., Kouyama, T., Sato, T. M., Takamura, M., Iwagami, N., Nakamura, M., Suzuki, M., Ueno, M.,

This article is protected by copyright. All rights reserved.

Author Manuscript

Author Manuscript

Hashimoto, G. L., Sato, M., Takagi, S., Yamazaki, A., Yamada, M., Murakami, S. Y., … Hirata, N. (2017). Absolute calibration of brightness temperature of the Venus disk observed by the Longwave Infrared Camera onboard Akatsuki Akatsuki at Venus: The First Year of Scientific Operation Masato Nakamura, Dmitri Titov, Kevin McGouldrick, Pierre Drossart, Jean-Lo. *Earth, Planets and Space*, *69*(1), 1–9. https://doi.org/10.1186/s40623-017-0727-y

Garate-Lopez, I., García Muñoz, A., Hueso, R., & Sánchez-Lavega, A. (2015). Instantaneous three-dimensional thermal structure of the South Polar Vortex of Venus. *Icarus*, *245*, 16–31. https://doi.org/10.1016/j.icarus.2014.09.030

García Muñoza, A., Millsa, F. P., Piccionic, G., & Drossart, P. (2009). The near-infrared nitric oxide nightglow in the upper atmosphere of Venus. *Proceedings of the National Academy of Sciences of the United States of America*, *106*(4), 985–988. https://doi.org/10.1073/pnas.0808091106

Gérard, J. C., Bougher, S. W., López-Valverde, M. A., Pätzold, M., Drossart, P., & Piccioni, G. (2017). Aeronomy of the Venus Upper Atmosphere. *Space Science Reviews*, *212*(3–4), 1617–1683. https://doi.org/10.1007/s11214-017-0422-0

Gérard, J. C., Cox, C., Soret, L., Saglam, A., Piccioni, G., Bertaux, J. L., & Drossart, P. (2009). Concurrent observations of the ultraviolet nitric oxide and infrared O 2 nightglow emissions with Venus Express. *Journal of Geophysical Research E: Planets*, *114*(9), 1–10. https://doi.org/10.1029/2009JE003371

Gérard, J. C., Saglam, A., Piccioni, G., Drossart, P., Cox, C., Erard, S., Hueso, R., & Sánchez-Lavega, A. (2008). Distribution of the O2 infrared nightglow observed with VIRTIS on

This article is protected by copyright. All rights reserved.

Author Manuscript

board Venus Express. *Geophysical Research Letters*, *35*(2), 1–5. https://doi.org/10.1029/2007GL032021

Gierasch, P. J., Goody, R. M., Young, R. E., Crisp, D., Edwards, C., Kahn, R., Rider, D., del Genio, A., Greeley, R., Hou, A., Leovy, C. B., McCleese, D., & Newman, M. (1997). The General Circualtion of the Venus Atmosphere: an Assessment. In S. W. Bougher, D. M. Hunten, & R. J. Phillips (Eds.), *Venus II: Geology, Geophysics, Atmosphere, and Solar Wind Environment* (p. 459). University of Arizona Press. https://ui.adsabs.harvard.edu/abs/1997veii.conf..459G

Gilli, G., Lebonnois, S., González-Galindo, F., López-Valverde, M. A., Stolzenbach, A., Lefèvre, F., Chaufray, J. Y., & Lott, F. (2017). Thermal structure of the upper atmosphere of Venus simulated by a ground-to-thermosphere GCM. *Icarus*, *281*, 55–72. https://doi.org/10.1016/j.icarus.2016.09.016

Gilli, G., López-Valverde, M. A., Peralta, J., Bougher, S., Brecht, A., Drossart, P., & Piccioni, G. (2015). Carbon monoxide and temperature in the upper atmosphere of Venus from VIRTIS/Venus Express non-LTE limb measurements. *Icarus*, *248*, 478–498. https://doi.org/10.1016/j.icarus.2014.10.047

Grassi, D., Drossart, P., Piccioni, G., Ignatiev, N. I., Zasova, L. V., Adriani, A., Moriconi, M. L., Irwin, P. G. J., Negrão, A., & Migliorini, A. (2008). Retrieval of air temperature profiles in the venusian mesosphere from VIRTIS-M data: Description and validation of algorithms. *Journal of Geophysical Research*, *113*(E9), 1–12. https://doi.org/10.1029/2008JE003075

Grassi, D., Migliorini, A., Montabone, L., Lebonnìois, S., Cardesìn-Moinelo, A., Piccioni, G., Drossart, P., & Zasova, L. V. (2010). Thermal structure of Venusian nighttime mesosphere

This article is protected by copyright. All rights reserved.

as observed by VIRTIS-Venus Express. *Journal of Geophysical Research E: Planets*, *115*(9), 1–11. https://doi.org/10.1029/2009JE003553

Grassi, D., Politi, R., Ignatiev, N. I., Plainaki, C., Lebonnois, S., Wolkenberg, P., Montabone, L., Migliorini, A., Piccioni, G., & Drossart, P. (2014). The Venus nighttime atmosphere as observed by the VIRTIS-M instrument. Average fields from the complete infrared data set. *Journal of Geophysical Research: Planets*, *119*(4), 837–849. https://doi.org/10.1002/2013JE004586

Haus, R., Kappel, D., & Arnold, G. (2014). Atmospheric thermal structure and cloud features in the southern hemisphere of Venus as retrieved from VIRTIS/VEX radiation measurements. *Icarus*, *232*, 232–248. https://doi.org/10.1016/j.icarus.2014.01.020

Häusler, B., Pätzold, M., Tyler, G. L., Barriot, J.-P., Bird, M. K., Dehant, V., Hinson, D. P., Simpson, R. A., Treumann, R. A., Eidel, W., Mattei, R., Rosenblatt, P., Remus, S., Selle, J., & Tellmann, S. (2007). Venus atmospheric, ionospheric, surface and interplanetary radio-wave propagation studies with the VeRa Radio Science experiment. *ESA Special Publication*, *SP 1295*, 1–30. http://sci.esa.int/science-e/www/object/index.cfm?fobjectid=41535

Häusler, B., Pätzold, M., Tyler, G. L., Simpson, R. A., Bird, M. K., Dehant, V., Barriot, J.-P., Eidel, W., Mattei, R., Remus, S., Selle, J., Tellmann, S., & Imamura, T. (2006). Radio science investigations by VeRa onboard the Venus Express spacecraft. *Planetary and Space Science*, *54*(13–14), 1315–1335. https://doi.org/10.1016/j.pss.2006.04.032

Hedin, A. E., Niemann, H. B., Kasprzak, W. T., & Seiff, A. (1983). Global empirical model of the Venus thermosphere. *Journal of Geophysical Research*, *88*(A1), 73.

This article is protected by copyright. All rights reserved.

Author Manuscript

https://doi.org/10.1029/JA088iA01p00073

Hinson, D. P., & Jenkins, J. M. (1995). Magellan radio occultation measurements of atmospheric waves on venus. In *Icarus* (Vol. 114, Issue 2, pp. 310–327). https://doi.org/10.1006/icar.1995.1064

Hoshino, N., Fujiwara, H., Takagi, M., & Kasaba, Y. (2013). Effects of gravity waves on the day-night difference of the general circulation in the Venusian lower thermosphere. *Journal of Geophysical Research E: Planets*, *118*(10), 2004–2015. https://doi.org/10.1002/jgre.20154

Hoshino, N., Fujiwara, H., Takagi, M., Takahashi, Y., & Kasaba, Y. (2012). Characteristics of planetary-scale waves simulated by a new venusian mesosphere and thermosphere general circulation model. *Icarus*, *217*(2), 818–830. https://doi.org/10.1016/j.icarus.2011.06.039

Hueso, R., Peralta, J., Garate-Lopez, I., Bandos, T. V., & Sánchez-Lavega, A. (2015). Six years of Venus winds at the upper cloud level from UV, visible and near infrared observations from VIRTIS on Venus Express. *Planetary and Space Science*, *113–114*, 78–99. https://doi.org/10.1016/j.pss.2014.12.010

Imai, M., Kouyama, T., Takahashi, Y., Yamazaki, A., Watanabe, S., Yamada, M., Imamura, T., Satoh, T., Nakamura, M., Murakami, S. ya, Ogohara, K., & Horinouchi, T. (2019). Planetary-Scale Variations in Winds and UV Brightness at the Venusian Cloud Top: Periodicity and Temporal Evolution. *Journal of Geophysical Research: Planets*, *Vmc*, 2635–2659. https://doi.org/10.1029/2019JE006065

Kasprzak, W. T., Hedin, A. E., Mayr, H. G., & Niemann, H. B. (1988). Wavelike perturbations observed in the neutral thermosphere of Venus. *Journal of Geophysical Research*, *93*(A10),

This article is protected by copyright. All rights reserved.

Author Manuscript

Author Manuscript

11237. https://doi.org/10.1029/ja093ia10p11237

Keating, G. M., Bertaux, J. L., Bougher, S. W., Dickinson, R. E., Cravens, T. E., Nagy, A. F., Hedin, A. E., Krasnopolsky, V. A., Nicholson, J. Y., Paxton, L. J., & von Zahn, U. (1985). Models of Venus neutral upper atmosphere: Structure and composition. *Advances in Space Research*, *5*(11), 117–171. https://doi.org/10.1016/0273-1177(85)90200-5

Kliore, A. J., & Patel, I. R. (1980). Vertical structure of the atmosphere of Venus from Pioneer Venus Orbiter radio occultations. *Journal of Geophysical Research*, *85*(A13), 7957. https://doi.org/10.1029/ja085ia13p07957

Kolosov, M. A., Yakovlev, O. I., Efimov, A. I., Matyugov, S. S., Timofeeva, T. S., Chub, E. V., Pavelyev, A. G., Kucheryavenkov, A. I., Kalashnikov, I. E., & Milekhin, O. E. (1980). Investigation of the Venus atmosphere and surface by the method of radiosounding using Venera-9 and 10 satellites. *Acta Astronautica*, *7*(2), 219–234. https://doi.org/10.1016/0094-5765(80)90062-4

Kostiuk, T., Livengood, T. A., Sonnabend, G., Fast, K. E., Hewagama, T., Murakawa, K., Tokunaga, A. T., Annen, J., Buhl, D., Schmülling, F., Luz, D., & Witasse, O. (2006). Stratospheric global winds on Titan at the time of Huygens descent. *Journal of Geophysical Research*, *111*(E7), E07S03. https://doi.org/10.1029/2005JE002630

Kostiuk, T., & Mumma, M. J. (1983). Remote sensing by IR heterodyne spectroscopy. *Applied Optics*, *22*(17), 2644. https://doi.org/10.1364/AO.22.002644

Kouyama, T., Imamura, T., Taguchi, M., Fukuhara, T., Sato, T. M., Yamazaki, A., Futaguchi, M., Murakami, S., Hashimoto, G. L., Ueno, M., Iwagami, N., Takagi, S., Takagi, M., Ogohara, K., Kashimura, H., Horinouchi, T., Sato, N., Yamada, M., Yamamoto, Y., …

This article is protected by copyright. All rights reserved.

Author Manuscript

Nakamura, M. (2017). Topographical and Local Time Dependence of Large Stationary Gravity Waves Observed at the Cloud Top of Venus. *Geophysical Research Letters*, *44*(24), 12,098-12,105. https://doi.org/10.1002/2017GL075792

Lee, C., & Richardson, M. I. (2010). A general circulation model ensemble study of the atmospheric circulation of Venus. *Journal of Geophysical Research E: Planets*, *115*(4), 1–11. https://doi.org/10.1029/2009JE003490

Lee, C., & Richardson, M. I. (2011). A discrete ordinate, multiple scattering, radiative transfer model of the venus atmosphere from 0.1 to 260 μm. *Journal of the Atmospheric Sciences*, *68*(6), 1323–1339. https://doi.org/10.1175/2011JAS3703.1

Lellouch, E., Goldstein, J., Rosenqvist, J., Bougher, S. W., & Paubert, G. (1994). Global Circulation, Thermal Structure, and Carbon Monoxide Distribution in Venus' Mesosphere in 1991. *Icarus*, *110*(2), 315–339. https://doi.org/10.1006/icar.1994.1125

Limaye, S. S., Lebonnois, S., Mahieux, A., Pätzold, M., Bougher, S., Bruinsma, S., Chamberlain, S., Clancy, R. T., Gérard, J. C., Gilli, G., Grassi, D., Haus, R., Herrmann, M., Imamura, T., Kohler, E., Krause, P., Migliorini, A., Montmessin, F., Pere, C., … Zasova, L. (2017). The thermal structure of the Venus atmosphere: Intercomparison of Venus Express and ground based observations of vertical temperature and density profiles☆. *Icarus*, *294*, 124–155. https://doi.org/10.1016/j.icarus.2017.04.020

Mahieux, A., Berkenbosch, S., Clairquin, R., Fussen, D., Mateshvili, N., Neefs, E., Nevejans, D., Ristic, B., Vandaele, A. C., Wilquet, V., Belyaev, D., Fedorova, A., Korablev, O., Villard, E., Montmessin, F., & Bertaux, J.-L. (2008). In-flight performance and calibration of SPICAV SOIR onboard Venus Express. *Applied Optics*, *47*(13), 2252.

This article is protected by copyright. All rights reserved.

https://doi.org/10.1364/AO.47.002252

Mahieux, A., Vandaele, A. C., Bougher, S. W., Drummond, R., Robert, S., Wilquet, V., Chamberlain, S., Piccialli, A., Montmessin, F., Tellmann, S., Pätzold, M., Häusler, B., & Bertaux, J. L. (2015b). Update of the Venus density and temperature profiles at high altitude measured by SOIR on board Venus Express. *Planetary and Space Science, 113–114*, 309–320. https://doi.org/10.1016/j.pss.2015.02.002

Mahieux, A., Vandaele, A. C., Robert, S., Wilquet, V., Drummond, R., López Valverde, M. A., López Puertas, M., Funke, B., & Bertaux, J. L. (2015a). Rotational temperatures of Venus upper atmosphere as measured by SOIR on board Venus Express. *Planetary and Space Science*, *113–114*, 347–358. https://doi.org/10.1016/j.pss.2014.12.020

Mahieux, A., Vandaele, A. C., Robert, S., Wilquet, V., Drummond, R., Montmessin, F., & Bertaux, J. L. (2012). Densities and temperatures in the Venus mesosphere and lower thermosphere retrieved from SOIR on board Venus Express: Carbon dioxide measurements at the Venus terminator. *Journal of Geophysical Research E: Planets*, *117*(7), 1–15. https://doi.org/10.1029/2012JE004058

Markiewicz, W. J., Titov, D. V., Limaye, S. S., Keller, H. U., Ignatiev, N., Jaumann, R., Thomas, N., Michalik, H., Moissl, R., & Russo, P. (2007). Morphology and dynamics of the upper cloud layer of Venus. *Nature*, *450*(7170), 633–636. https://doi.org/10.1038/nature06320

Migliorini, A., Grassi, D., Montabone, L., Lebonnois, S., Drossart, P., & Piccioni, G. (2012). Investigation of air temperature on the nightside of Venus derived from VIRTIS-H on board Venus-Express. *Icarus*, *217*(2), 640–647. https://doi.org/10.1016/j.icarus.2011.07.013

This article is protected by copyright. All rights reserved.

Author Manuscript

Nakagawa, H., Hoshino, N., Sornig, M., Kasaba, Y., Sonnabend, G., Stupar, D., Aoki, S., & Murata, I. (2013). Comparison of general circulation model atmospheric wave simulations with wind observations of venusian mesosphere. *Icarus*, *225*(1), 840–849. https://doi.org/10.1016/j.icarus.2013.02.029

Nara, Y., Imamura, T., Murakami, S., Kouyama, T., Ogohara, K., Yamada, M., Takagi, M., Kashimura, H., & Sato, N. (2019). Formation of the Y Feature at the Venusian Cloud Top by Planetary-Scale Waves and the Mean Circulation: Analysis of Venus Express VMC Images. *Journal of Geophysical Research: Planets*, *124*(5), 1143–1156. https://doi.org/10.1029/2018JE005779

Niemann, H. B., Kasprzak, W. T., Hedin, A. E., Hunten, D. M., & Spencer, N. W. (1980). Mass spectrometric measurements of the neutral gas composition of the thermosphere and exosphere of Venus. *Journal of Geophysical Research*, *85*(A13), 7817. https://doi.org/10.1029/ja085ia13p07817

Ohtsuki, S., Iwagami, N., Sagawa, H., Kasaba, Y., Ueno, M., & Imamura, T. (2005). Ground-based observation of the Venus 1.27-μm O 2 airglow. *Advances in Space Research*, *36*(11), 2038–2042. https://doi.org/10.1016/j.asr.2005.05.078

Ohtsuki, S., Iwagami, N., Sagawa, H., Ueno, M., Kasaba, Y., Imamura, T., & Nishihara, E. (2008). Imaging spectroscopy of the Venus 1.27-μm O 2 airglow with ground-based telescopes. *Advances in Space Research*, *41*(9), 1375–1380. https://doi.org/10.1016/j.asr.2007.10.014

Parkinson, C. D., Bougher, S. W., Brecht, A. S., & Gilli, G. (2019). The impact of Venus middle atmosphere aerosol heating upon SO2 and CO density distributions through GCM model

This article is protected by copyright. All rights reserved.

Author Manuscript

Author Manuscript

simulations. *International Venus Conference*, Niseko, Hokkaido, Japan.

Peralta, J., Hueso, R., & Sánchez-Lavega, A. (2007). Cloud brightness distribution and turbulence in Venus using Galileo violet images. *Icarus*, *188*(2), 305–314. https://doi.org/10.1016/j.icarus.2006.12.005

Peralta, J., Hueso, R., Sánchez-Lavega, A., Piccioni, G., Lanciano, O., & Drossart, P. (2009). Characterization of mesoscale gravity waves in the upper and lower clouds of Venus from VEX-VIRTIS images. *Journal of Geophysical Research E: Planets*, *113*(5), 1–12. https://doi.org/10.1029/2008JE003185

Piccialli, A., Montmessin, F., Belyaev, D., Mahieux, A., Fedorova, A., Marcq, E., Bertaux, J. L., Tellmann, S., Vandaele, A. C., & Korablev, O. (2015). Thermal structure of Venus nightside upper atmosphere measured by stellar occultations with SPICAV/Venus Express. *Planetary and Space Science*, *113–114*, 321–335. https://doi.org/10.1016/j.pss.2014.12.009

Piccialli, A., Titov, D. V., Sanchez-Lavega, A., Peralta, J., Shalygina, O., Markiewicz, W. J., & Svedhem, H. (2014). High latitude gravity waves at the Venus cloud tops as observed by the Venus Monitoring Camera on board Venus Express. *Icarus*, *227*, 94–111. https://doi.org/10.1016/j.icarus.2013.09.012

Piccioni, G., Zasova, L., Migliorini, A., Drossart, P., Shakun, A., Munoz, A. G., Mills, F. P., & Cardesin-Moinelo, A. (2009). Near-IR oxygen nightglow observed by VIRTIS in the Venus upper atmosphere. *Journal of Geophysical Research E: Planets*, *114*(5), 1–18. https://doi.org/10.1029/2008JE003133

Rengel, M., Hartogh, P., & Jarchow, C. (2008). HHSMT observations of the Venusian mesospheric temperature, winds, and CO abundance around the MESSENGER flyby.

This article is protected by copyright. All rights reserved.

Planetary and Space Science, *56*(13), 1688–1695. https://doi.org/10.1016/j.pss.2008.07.014

Rossow, W. B., Del Genio, A. D., & Eichler, T. (1990). Cloud-Tracked Winds from Pioneer Venus OCPP Images . In *Journal of the Atmospheric Sciences* (Vol. 47, Issue 17, pp. 2053–2084). https://doi.org/10.1175/1520-0469(1990)047<2053:ctwfvo>2.0.co;2

Rossow, W. B., Del Genio, A. D., Limaye, S. S., Travis, L. D., & Stone, P. H. (1980). Cloud morphology and motions from Pioneer Venus images. *Journal of Geophysical Research*, *85*(A13), 8107. https://doi.org/10.1029/ja085ia13p08107

Schubert, G. (1983). General circulation and the dynamical state of the Venus atmosphere. In *Venus* (pp. 681–765). University of Arizona Press. https://ui.adsabs.harvard.edu/abs/1983vens.book..681S

Seiff, A., Kirk, D. B., Young, R. E., Blanchard, R. C., Findlay, J. T., Kelly, G. M., & Sommer, S. C. (1980). Measurements of thermal structure and thermal contrasts in the atmosphere of Venus and related dynamical observations: Results From the four Pioneer Venus Probes. *Journal of Geophysical Research*, *85*(A13), 7903. https://doi.org/10.1029/ja085ia13p07903

Sonnabend, G., Kroetz, P., Sornig, M., & Stupar, D. (2010). Direct observations of Venus upper mesospheric temperatures from ground based spectroscopy of CO2. *Geophysical Research Letters*, *37*(11), 10–13. https://doi.org/10.1029/2010GL043335

Soret, L., Gérard, J. C., Montmessin, F., Piccioni, G., Drossart, P., & Bertaux, J. L. (2012). Atomic oxygen on the Venus nightside: Global distribution deduced from airglow mapping. *Icarus*, *217*(2), 849–855. https://doi.org/10.1016/j.icarus.2011.03.034

Sornig, M., Livengood, T. A., Sonnabend, G., Stupar, D., & Kroetz, P. (2012). Direct wind measurements from November 2007 in Venus' upper atmosphere using ground-based

This article is protected by copyright. All rights reserved.

Author Manuscript

heterodyne spectroscopy of CO 2 at 10μm wavelength. *Icarus*, *217*(2), 863–874. https://doi.org/10.1016/j.icarus.2011.03.019

Sornig, M., Livengood, T., Sonnabend, G., Kroetz, P., Stupar, D., Kostiuk, T., & Schieder, R. (2008). Venus upper atmosphere winds from ground-based heterodyne spectroscopy of CO2 at wavelength. *Planetary and Space Science*, *56*(10), 1399–1406. https://doi.org/10.1016/j.pss.2008.05.006

Tellmann, S., Häusler, B., Hinson, D. P., Tyler, G. L., Andert, T. P., Bird, M. K., Imamura, T., Pätzold, M., & Remus, S. (2012). Small-scale temperature fluctuations seen by the VeRa Radio Science Experiment on Venus Express. *Icarus*, *221*(2), 471–480. https://doi.org/10.1016/j.icarus.2012.08.023

Titov, D., Markiewicz, W., Ignatiev, N., Song, L., Limaye, S. S., Sanchez-Lavega, A., Hesemann, J., Almeida, M., Roatsch, T., Matz, K. D., Scholten, F., Crisp, D., Esposito, L., Hviid, S. F., Jaumann, R., Keller, H. U., & Moissl, R. (2012). Morphology of the cloud tops as observed by the Venus Express Monitoring Camera. *Icarus*, *217*(2), 682–701. https://doi.org/10.1016/j.icarus.2011.06.020

Vandaele, A. C., Mahieux, A., Chamberlain, S., Ristic, B., Robert, S., Thomas, I. R., Trompet, L., Wilquet, V., & Bertaux, J. L. (2016). Carbon monoxide observed in Venus' atmosphere with SOIR/VEx. *Icarus*, *272*, 48–59. https://doi.org/10.1016/j.icarus.2016.02.025

Vandaele, A. C., Mahieux, A., Robert, S., Berkenbosch, S., Clairquin, R., Drummond, R., Letocart, V., Neefs, E., Ristic, B., Wilquet, V., Colomer, F., Belyaev, D., & Bertaux, J. L. (2013). Improved calibration of SOIR/Venus Express spectra. *Optics Express*, *21*(18), 21148. https://doi.org/10.1364/OE.21.021148

This article is protected by copyright. All rights reserved.

Author Manuscript

Vandaele, A. C., Mahieux, A., Robert, S., Drummond, R., Wilquet, V., & Bertaux, J. L. (2015). Carbon monoxide short term variability observed on Venus with SOIR/VEX. *Planetary and Space Science*, *113–114*, 237–255. https://doi.org/10.1016/j.pss.2014.12.012

Zalucha, A. M., Brecht, A. S., Rafkin, S., Bougher, S. W., & Alexander, M. J. (2013). Incorporation of a gravity wave momentum deposition parameterization into the Venus Thermosphere General Circulation Model (VTGCM). *Journal of Geophysical Research E: Planets*, *118*(1), 147–160. https://doi.org/10.1029/2012JE004168

Zhang, S., Bougher, S. W., & Alexander, M. J. (1996). The impact of gravity waves on the Venus thermosphere and O2 IR nightglow. *Journal of Geophysical Research E: Planets*, *101*(E10), 23195–23205. https://doi.org/10.1029/96JE02035

Author Manuscript

This article is protected by copyright. All rights reserved.

Author Manuscript

Simulation #	Lower Boundary	Wave	Wave GH [m]
1	uniform	Rossby	10
2	uniform	Kelvin	110
3	OXLB	Rossby	10
4	OXLB	Kelvin	50
5	OXLB	Rossby + Kelvin	10/50

Table 1: Summary of VTGCM simulations and their conditions/parameters. The uniform is related to the VTGCM simulations lower boundary conditions being T= 250K and U=V=0. The OXLB is related to the VTGCM simulations with the Oxford GCM T, U, V, GH output at a given pressure slice as the lower boundary. See section 2 for more details.

Rossby Wave Cases						Kelvin Wave Cases					
Sim.	Tmax (K)	Alt (km)	Umax (m/s)	Alt (km)	Peak Propag. Alt (km)	Sim.	Tmax (K)	Alt (km)	Umax (m/s)	Alt (km)	Peak Propag. Alt (km)
H12	0.4	95	0.6	105	130	H12	2.5	95	6.0	105	130
1	0.1	92	0.8	81	118	2	3.0	94	6.0	89	125
3	3.0	81	4.8	91	118	4	13.8	92	23.4	103	125
5 (RW+KW)	13.3	92	22.5	102	125	5 (RW+KW)	13.3	92	22.5	102	125

Table 2: Summary of maximum fluctuations in temperature (K) and zonal wind (m/s) and their respective altitude near the equator. See text for description of calculating these values from 60 Earth day simulations. The left 6 columns are the Rossby wave cases, where "Tmax" is the maximum temperature amplitude with its respective altitude ("Alt"), "Umax" is the maximum zonal wind amplitude with its respective altitude ("Alt"), and "Peak Propag. Alt" is the highest altitude of wave propagation. The right 6 columns represent the Kelvin waves cases. The bottom row of both sides represents the simulation with both Rossby and Kelvin waves (#5).

This article is protected by copyright. All rights reserved.

Author Manuscript

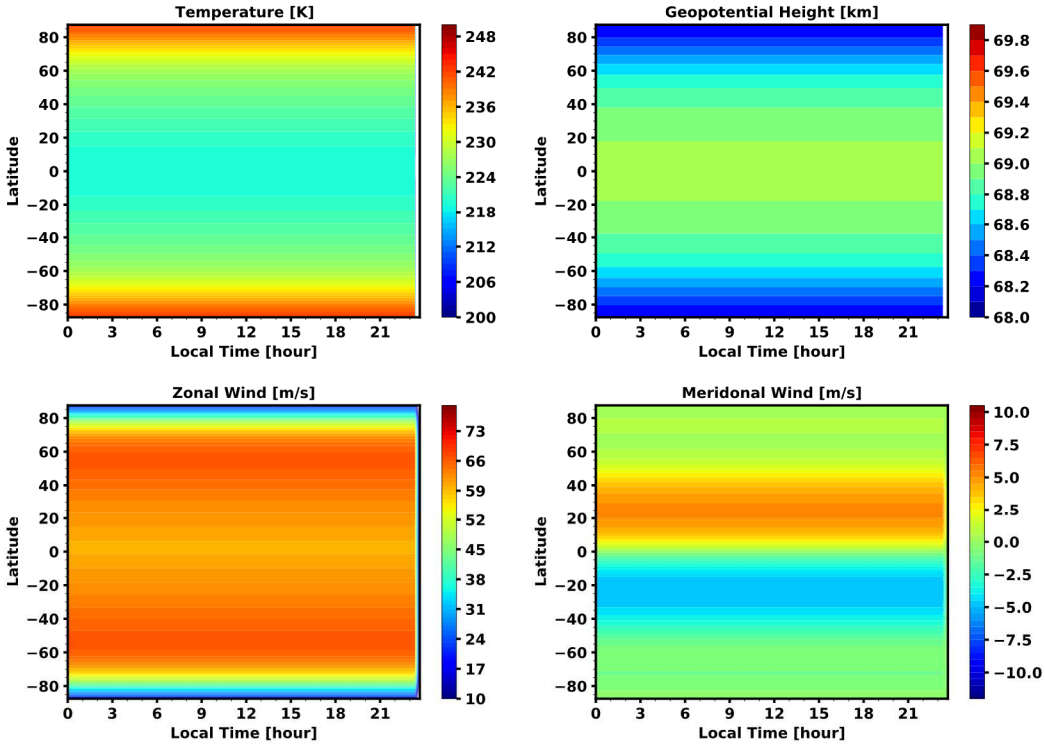

Figure 1: VTGCM lower boundary; zonally and 5 day averaged pressure slices (4.44 x 10^3 Pa) for temperature (K), geopotential height (km), zonal wind (m/s), and meridional wind (m/s). From the Oxford Venus GCM (Lee and Richardson, 2010; 2011).

This article is protected by copyright. All rights reserved.

Author Manuscript

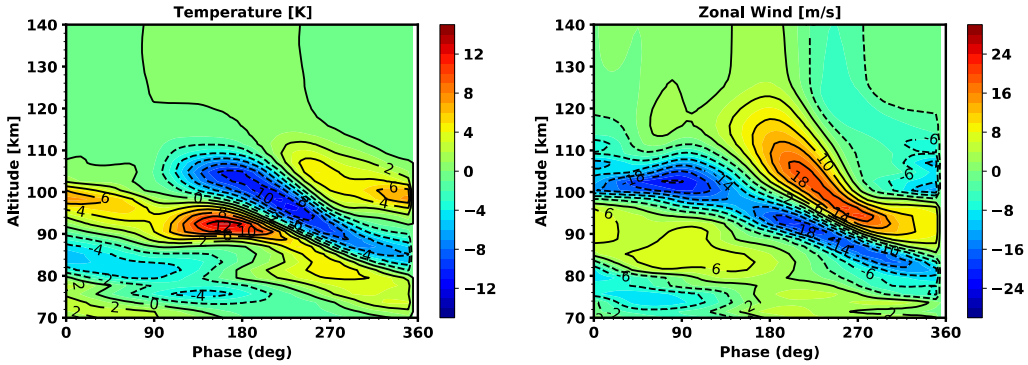

This article is protected by copyright. All rights reserved.

Author Manuscript

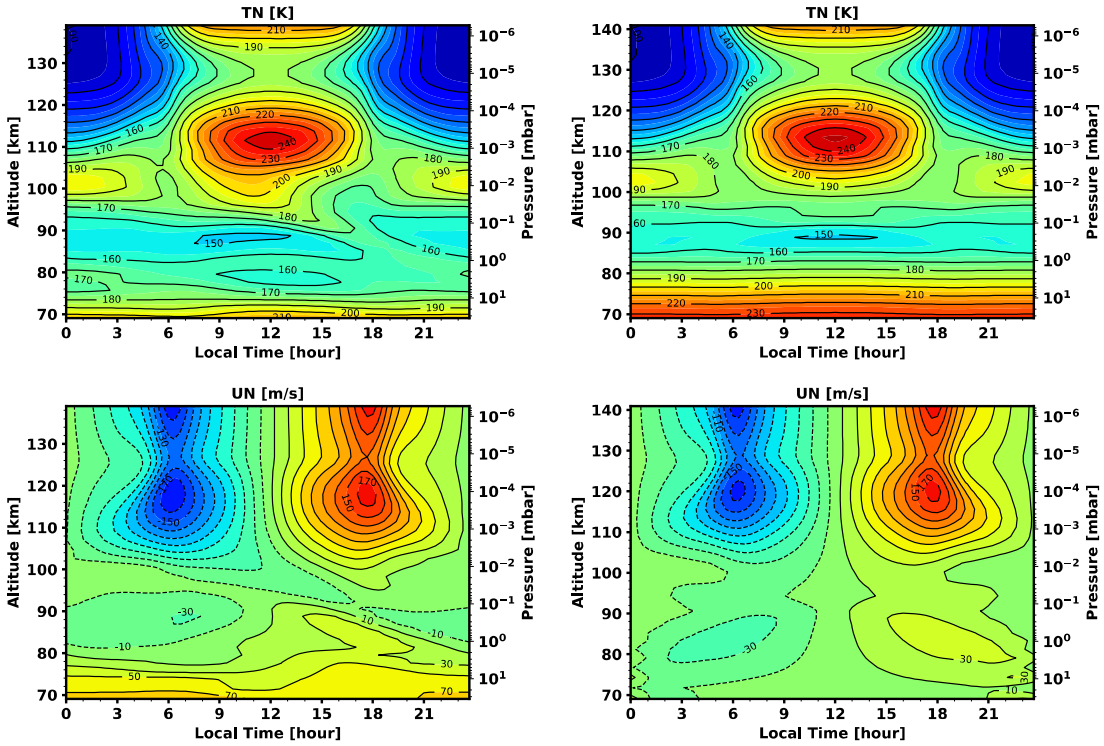

Figure 3: Temperature (K) (top) and zonal wind (m/s) (bottom) equatorial slices from simulation #5 of the last timestep [left two panels]. The right two panels are the difference between the last timestep of simulation #5 and the starting history. Longitude-height cross section at 2.5° N (local time versus height). Positive zonal wind values are westward and negative zonal wind values are eastward [Venus convention]. *Contour line intervals going clockwise starting at top left panel: 10 K, 5 K, 20 m/s, and 20 m/s.*

This article is protected by copyright. All rights reserved.

Author Manuscript

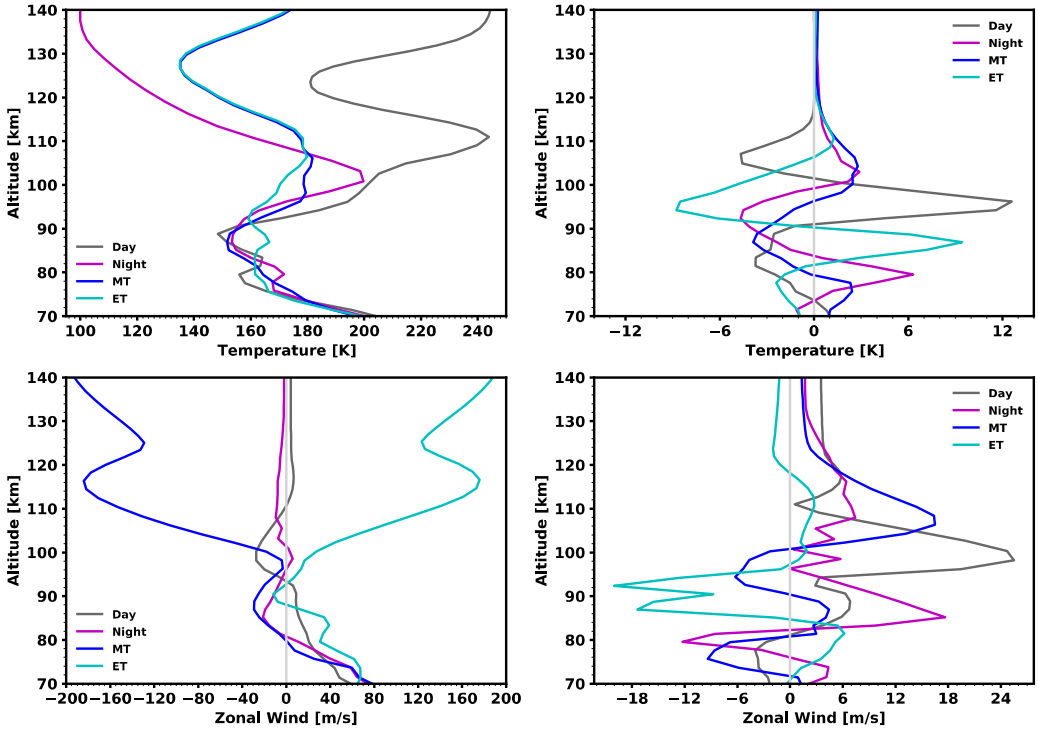

Figure 4: Temperature (K) (top) and Zonal wind (m/s) (bottom) vertical profiles at the equator (Lat = 0°) from simulation #5. The left panels are dayside (LT = 12), nightside (LT = 00), evening terminator (ET), and morning terminator (MT) profiles. The right panels show the difference between simulation #5 with planetary waves and without planetary waves for all four local times. For zonal wind, the absolute value was taken before subtracting them. The positive values represent the wave case is faster and the negative represents the no wave case is faster.

This article is protected by copyright. All rights reserved.

Author Manuscript

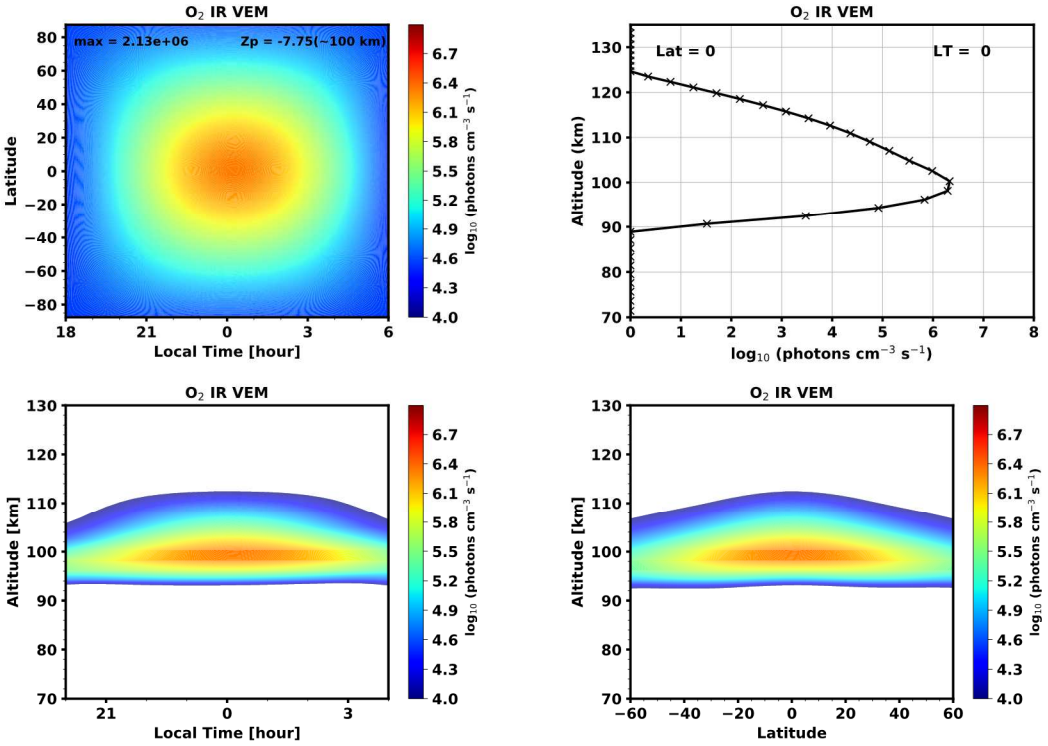

Figure 5: O_2 IR nightglow volume emission rate (VEM) close to midnight from the end of simulation #5. The emission rate unit is Log_{10} (photons cm^{-3} s^{-1}). Left panel is local time-latitude cross section at 2.5° N at ~100 km. The maximum emission is equal to 2.13e6 photons cm^{-3} s^{-1}. The right side is emission-height profile, where the peak emission occurs at ~100km. Bottom left panel is VEM on an altitude vs LT cross section (constant LAT = 2.5N), while bottom right panel is VEM on an altitude vs Latitude slice (constant LT = 0.0).

This article is protected by copyright. All rights reserved.

Author Manuscript

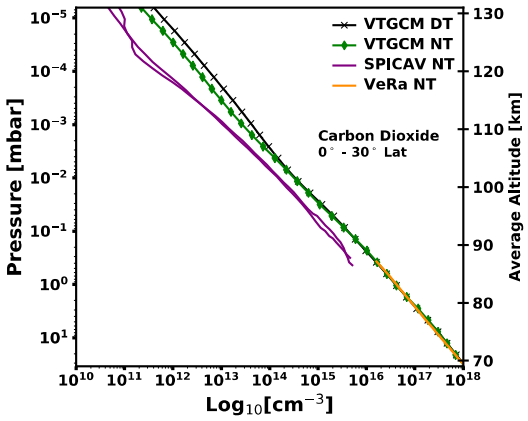

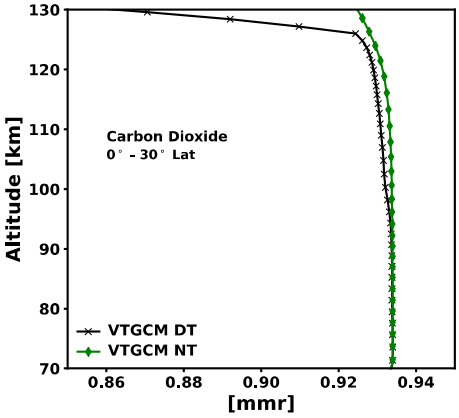

This article is protected by copyright. All rights reserved.

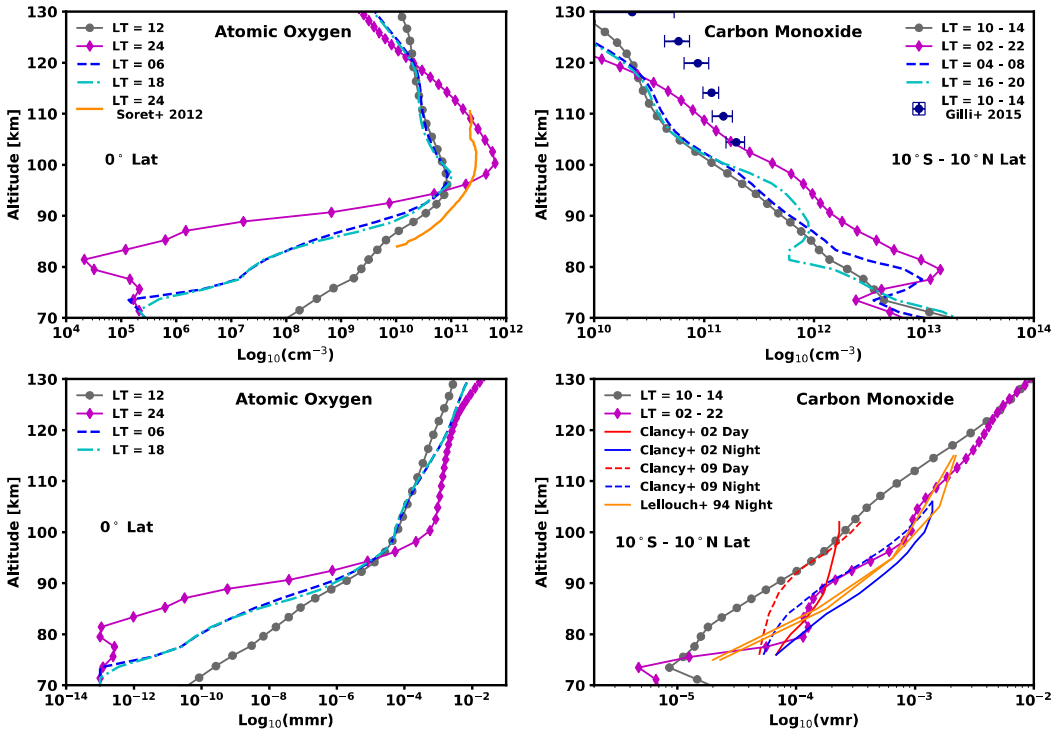

Figure 7: Vertical profiles of atomic oxygen and carbon monoxide from simulation #5 (simulation #5 without waves are not represented for clarity purposes). [Top left] Vertical profiles of atomic oxygen in number density (cm^{-3}) at the equator at LT = 06, 12, 18, 24 with the derived [O] profile from VIRTIS VEX O_2 IR nightglow observations at LT = 24 and Lat = 0° (Soret et al., 2012). [Top right] Vertical profiles of carbon monoxide in number density (cm^{-3}) are averaged over 10°S - 10°N for LT bins as specified in the legend. The VIRITS-H observations from Gilli et al. 2015 (purple dot with respective error bars) for the averaged box of Latitude = 10S – 10N and LT = 10hr – 14hr is represented for comparisons. [Bottom left] Vertical profiles of atomic oxygen in mass mixing ratio at the equator at LT = 06, 12, 18, 24. [Bottom right] Vertical profiles of carbon monoxide observations in volume mixing ratio averaged over 10°S - 10°N for LT bins as specified in the legend. Clancy et al. (2012) CO observations are dashed and solid for the two different observing campaigns and the profiles represent disk averages. The two solid orange lines represent two different beam positions (LT = 23, Lat = 8 and LT = 22, Lat = -10) from Lellouch et al., 1994.

This article is protected by copyright. All rights reserved.

Author Manuscript

Author Manuscript

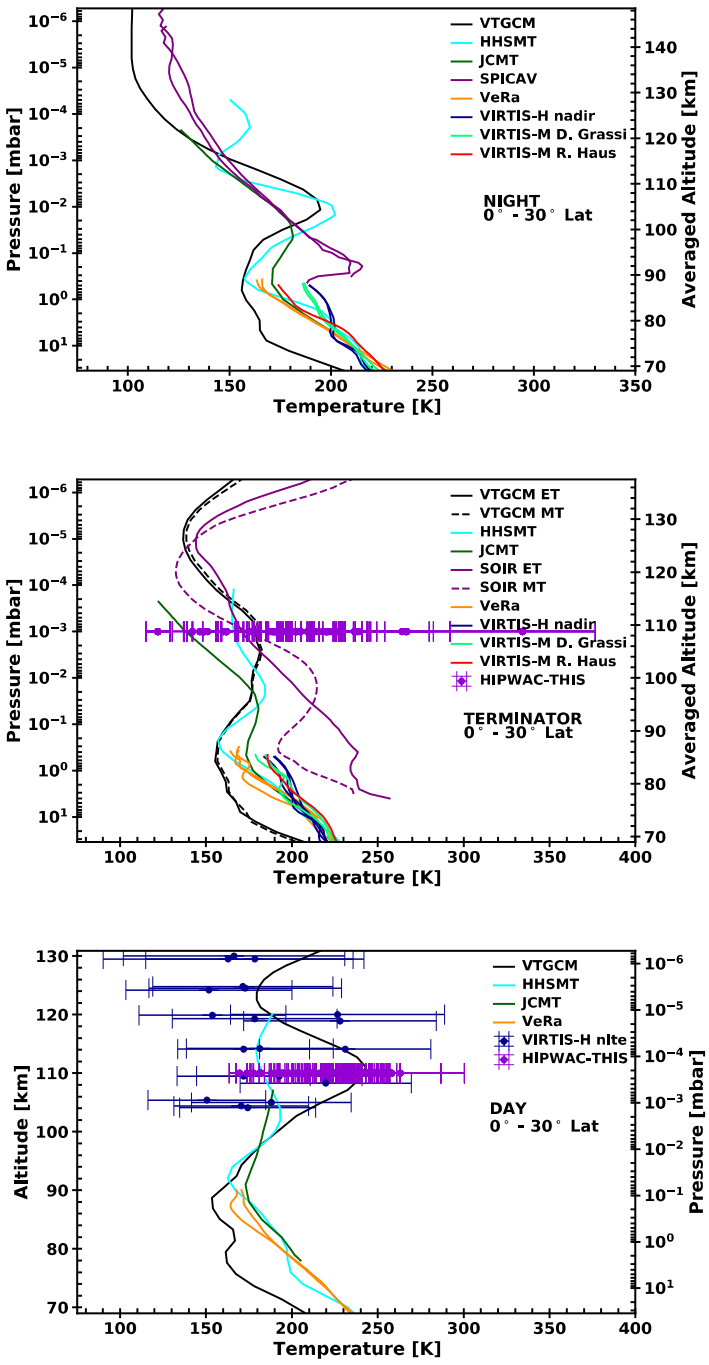

CM and observations near the equator
is terminator, and bottom panel is day
ays of the "combined case" with the
shadowing representing the maximum and minimum value during the last four days at that specific vertical level. The observations are from the Venus Express instruments and ground-based observations. The shadowing around the observation profiles represent averged profiles uncertainties, while the error bars are used for individual observations uncertainties.

This article is protected by copyright. All rights reserved.

Author Manuscript

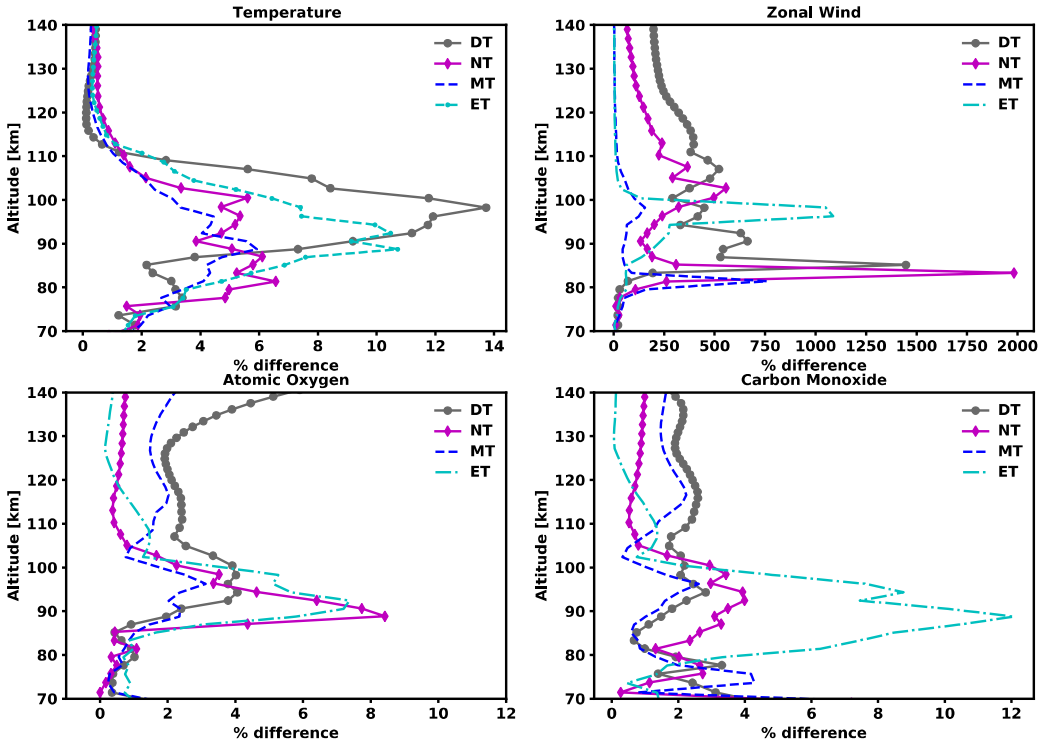

Figure 9: The percent relative difference between the minimum and maximum value at each altitude over 4 Earth days near the equator from simulation #5. The top left is temperature, top right is zonal wind, bottom left is atomic oxygen, and bottom right is carbon monoxide. Each panel represents daytime (DT), nighttime (NT), evening terminator (ET), and morning terminator (MT) for a averaged latitude bin of 0° to 30°.

This article is protected by copyright. All rights reserved.

Author Manuscript

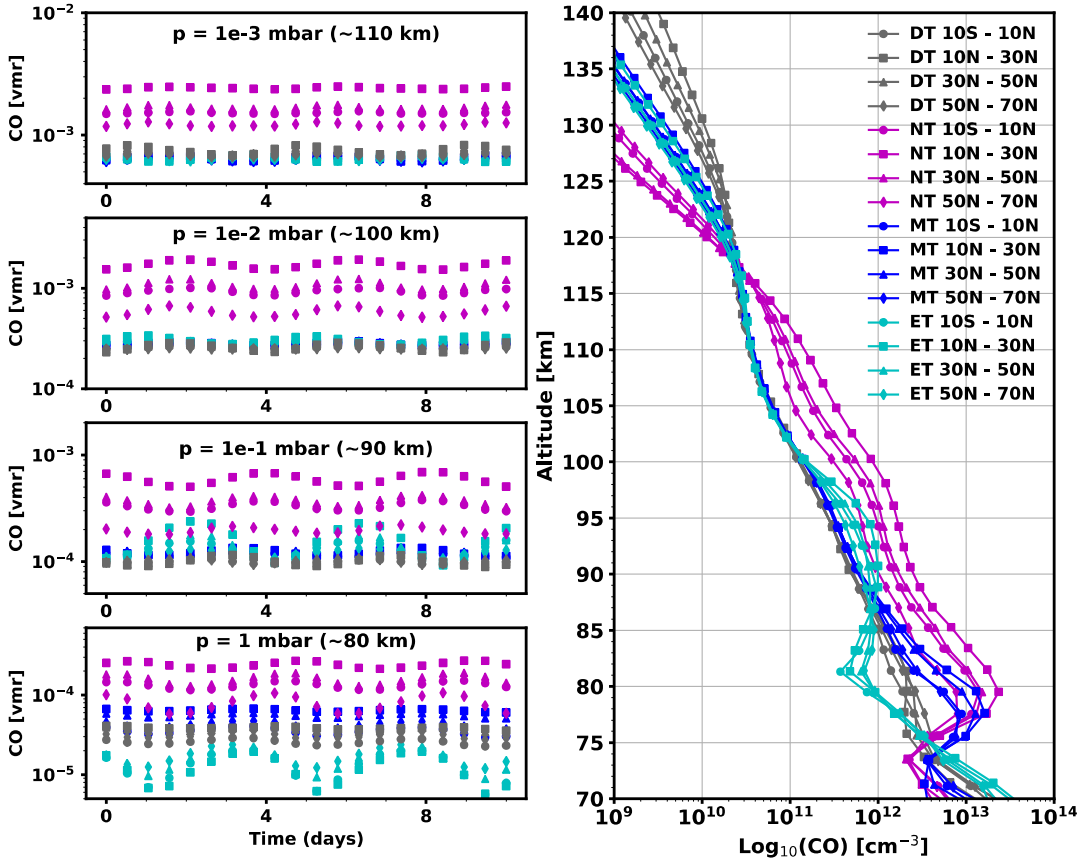

Figure 10: Four left panels represent CO volume mixing ratio versus simulation time (last 10 days of simulation #5). The right panel is altitude versus log10(CO) density (cm-3). The colors represent average local time (LT) bins: DT = 10-14hr, NT = 02-22 hr, MT = 04-08 hr, ET = 16-20 hr. The symbols represent averaged latitude bins as marked in the legend of the right panel.

This article is protected by copyright. All rights reserved.

Author Manuscript

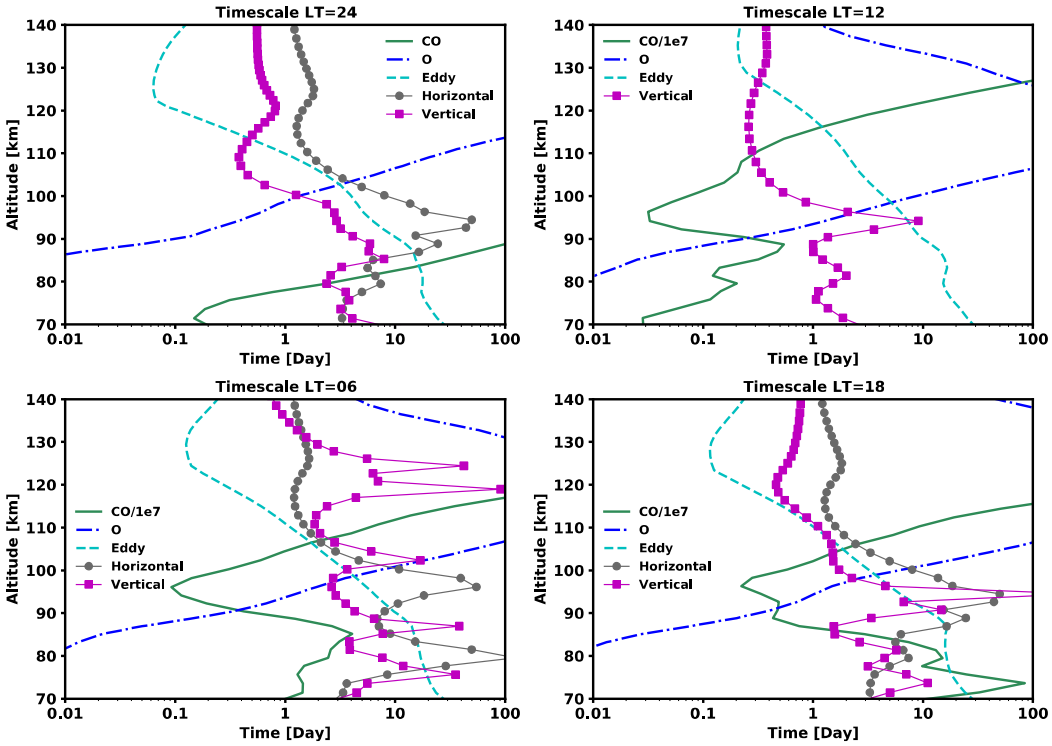

Figure 11: Timescales profiles at 2.5° N (time (Day) versus height (km)) for LT = 06, 12, 18, and 24.

This article is protected by copyright. All rights reserved.

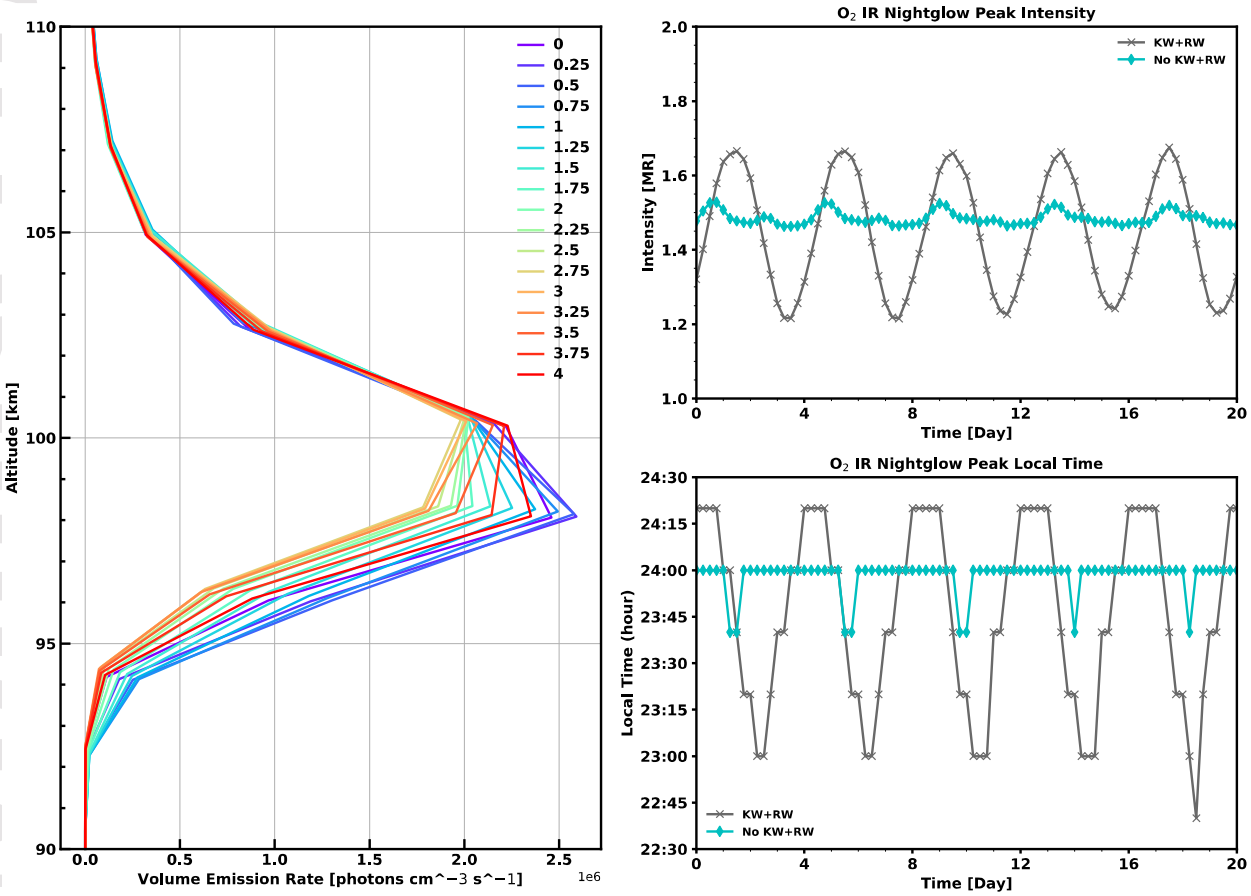

Figure 12: O_2 IR nightglow volume emission rate (VER) variations. The left panel is vertical profiles of the peak VER for the last four days of simulation #5. The colors are associated to the time (hours) and are correlated to the x-axis of the two panels on the right. The VER unit is ($x10^6$ photons cm^{-3} s^{-1}). The top right panel shows temporal variations of the peak O_2 IR nightglow integrated intensity (MR) over the last 20 of 60 day simulation #5. The bottom right panel shows the temporal variations of the peak VER local time (hours). The cyan-diamond line is the case without planetary waves. The grey star line represents the case with planetary waves.

Author Manuscript

This article is protected by copyright. All rights reserved.